Journal of Geochemical Exploration 280 (2026) 107906

Contents lists available at ScienceDirect

Journal of Geochemical Exploration

journal homepage: www.elsevier.com/locate/gexplo

GEMAS: Novel continental-scale patterns revealed in the spatial distribution of Cr in European agricultural soil – A systematic method validation

Attila Petrik [a], Gyozo Jordan [b], Ahmed Abdelaal [c,*], Alecos Demetriades [d,1], Benedetto De Vivo [e,h,i,1], Stefano Albanese [f], Martiya Sadeghi [g], The GEMAS Project Team [2]

[a] Eriksfiord AS, Professor Olav Hanssensvei 7A, 4021, Stavanger, Norway
[b] Geological Survey of Finland, Vuorimiehentie 5, 02151, Espoo, Finland
[c] Environmental Sciences Department, Faculty of Science, Port Said University, Port Said, 42522, Egypt
[d] Institute of Geology and Mineral Exploration, Athens, Hellenic Republic
[e] University of Napoli Federico II, Italy
[f] Department of Earth Sciences, Environment and Resources, University of Naples Federico II, Via Cupa Cintia 21, 80126, Naples, Italy
[g] Geological Survey of Sweden, SE-751 28, Uppsala, Sweden
[h] Virginia Tech, Blacksburg, VA, USA
[i] Nanjing University, Nanjing and Hubei Polytechnic University, Huangshi, China

ARTICLE INFO

Keywords:
Univariate statistics
Digital Image Processing
Spatial features
Residual pattern
Ratio map
Triangular irregular networks (TIN)
Lithology

ABSTRACT

Following the Ni-focused experimental investigation, it was clear that a critical advancement in digital image analysis of geochemical data sets required the validation of the procedures used with another element. Chromium was selected because its geochemical behaviour closely mirrors that of Ni in both lithological context and surface processes. Our current study, conducted with rigorous methodological precision, aims to assess a novel geospatial technique capable of capturing spatially variable continental-scale element distribution patterns. To reduce localised anomalies, we applied a moving average filter to the TIN-based interpolated Cr data set. The processed grid was then subjected to digital image analysis, which highlighted several continental-scale spatial orientations — NE-SW, E-W, and NW-SE — that closely resemble those found in the Ni study. Notably, prominent NE-SW and ENE-WSW linear Cr structures were identified, aligning with the known structural imprints of the Variscan and Alpine orogenic belts. Elevated Cr variable concentrations mainly occur in the Balkans and Alpine regions, consistent with exposures of mafic to ultramafic lithologies. A striking east-west trending Cr feature, with lower concentrations northwards, was also observed within the terminal zone of the last major glaciation, aligning with Cr-depleted glaciofluvial deposits. Chromium anomalies with a NW-SE trend also occur in regions such as Fennoscandia, Hellenic Republic, northern Italy, and the Pyrenees, aligning with those for Ni. Beyond confirming the efficacy of image analysis techniques in uncovering and describing new geochemical spatial patterns, this research also reinforces the approach by showing a pronounced continental-scale spatial correspondence between Cr and Ni distributions.

* Corresponding author.
E-mail address: ahmed_abdelaal@sci.psu.edu.eg (A. Abdelaal).
[1] Retired.
[2] The GEMAS Project Team: M. Andersson, R. Baritz, M.J. Batista, A. Bel-lan, M. Birke, D. Cicchella, W. De Vos, E. Dinelli, M. Ďuriš, A. Dusza-Dobek, O.A. Eggen, M. Eklund, V. Ernstsen, P. Filzmoser, D.M.A. Flight, S. Forrester, M. Fuchs, U. Fügedi, A. Gilucis, M. Gosar, V. Gregorauskiene, W. De Groot, A. Gulan, J. Halamić, E. Haslinger, P. Hayoz, R. Hoffmann, J. Hoogewerff, H. Hrvatovic, S. Husnjak, L. Janik, J. Kirby, V. Klos, F. Krone, P. Kwecko, L. Kuti, A. Ladenberger, A. Lima, J. Locutura, P. Lucivjansky, A. Mann, D. Mackovych, M. McLaughlin, B.I. Malyuk, R. Maquil, R.G. Meuli, G. Mol, P. Négrel, P. O'Connor, K. Oorts, A. Pasieczna, S. Pfleiderer, M. Poňavič, C. Prazeres, U. Rauch, S. Radusinović, C. Reimann, I. Salpeteur, R. Scanlon, A. Schedl, A. Scheib, I. Schoeters, E. Sellersjö, I. Slaninka, J.M. Soriano-Disla, A. Šorša, R. Svrkota, T. Stafilov, T. Tarvainen, V. Trendavilov, P. Valera, V. Verougstraete, D. Vidojević and Z. Zomeni.

https://doi.org/10.1016/j.gexplo.2025.107906
Received 10 May 2025; Received in revised form 9 September 2025; Accepted 10 September 2025
Available online 13 September 2025

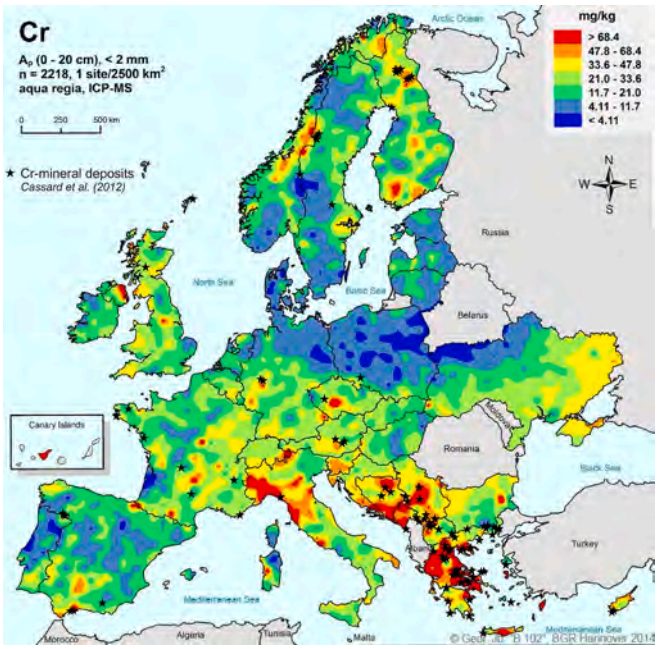

Fig. 1. Colour-surface map showing the spatial distribution of hot aqua regia extractable Cr concentrations in European agricultural (Ap) topsoil (0–20 cm) samples taken from the Geochemical Mapping of Agricultural and Grazing Land Soil Atlas (Reimann et al., 2014a, 2014b). The Cr-mineral deposits are also displayed after Cassard et al. (2012, 2015). (For interpretation of the references to colour in this figure legend, the reader is referred to the web version of this article). (For interpretation of the references to colour in this figure legend, the reader is referred to the web version of this article.)

1. Introduction

The project of Geochemical Mapping of Agricultural and Grazing Land Soil (GEMAS) developed a harmonised, continent-wide geochemical database according to the specifications of the European Union's REACH regulation (Registration, Evaluation, and Authorization of Chemicals; EC, 2006; Reimann et al., 2014a, 2014b). Numerous investigations have examined the spatial element distribution within this data set, linking patterns to mineral provinces, geological substrates, historical glacial extent, climatic influences, and human-related contamination sources (Reimann et al., 2012, 2014a, 2014b; Scheib et al., 2012, 2014; Tarvainen et al., 2013; Fabian et al., 2014; Albanese et al., 2015; Birke et al., 2014, 2017; Négrel et al., 2019). For instance, Cr levels in surface agricultural soil, as presented in the GEMAS *Chemistry of Europe's Agricultural Soil Atlas* (Fig. 1) (Reimann et al., 2014a), exhibit a pronounced latitudinal divide: lower concentrations are generally observed in northern Europe, while higher concentrations prevail in the south. This boundary coincides with the terminal margin of the last major glaciation, a relationship noted by many researchers (Salminen et al., 2005; De Vos et al., 2006; Scheib et al., 2012, 2014; Reimann et al., 2014c; Albanese et al., 2015). Elevated Cr values are particularly clustered in the Balkans and northern Italy (Alps and Apennines), reflecting the occurrence of mafic and ultramafic rock formations. The high Cr concentrations in the Balkans are further associated with significant mineralisation in the region (Fig. 1).

Chromium ranks as the 23rd most prevalent element in the Earth's upper continental crust, with a typical abundance of 73 mg/kg (Hu and Gao, 2008). It is a lithophile metallic element predominantly found in chromite ($FeCr_2O_4$) and, more rarely, crocoite ($PbCrO_4$), and also occurs as a minor component in minerals such as amphibole, garnet, spinel, mica (fuchsite), and pyroxene (Kabata-Pendias and Pendias, 2001). Due to similar ionic radii, Cr^{3+} readily substitutes for Fe and Mg and enters early formed minerals like pyroxene and spinel during magmatic differentiation (Hseu et al., 2018). Consequently, ultramafic rocks, often rich in other metals such as Ni, serve as a major source of Cr (Albanese et al., 2015; Delina et al., 2020). In addition to chromite, basaltic melts often transport Cr, with elevated levels observed in magnetite and ilmenite phases (Wedepohl, 1978). According to Mielke (1979), Cr concentrations vary by igneous rock type: approximately 1600 mg/kg in ultramafic, 170 mg/kg in basaltic, and 4–22 mg/kg in granitic rocks. Chromium-bearing heavy minerals such as chromite may accumulate in placer deposits alongside magnetite, zircon, rutile, cassiterite, monazite,

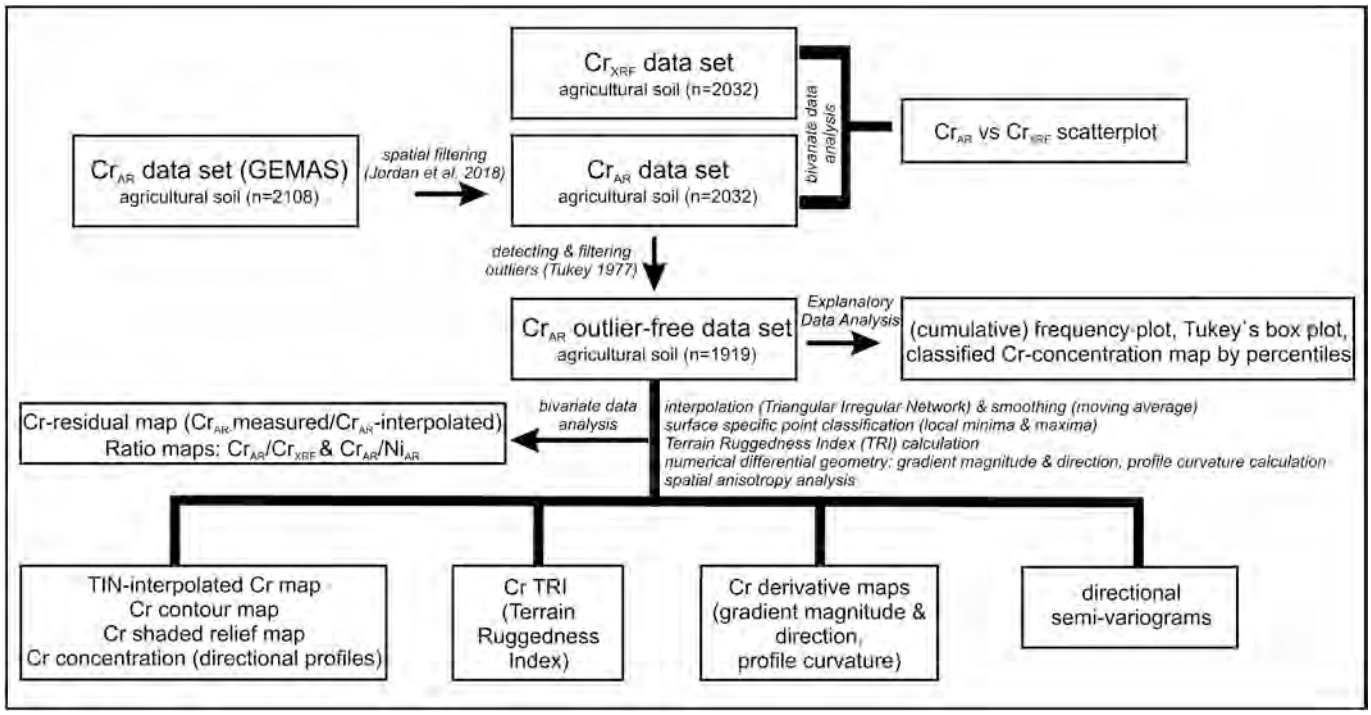

Fig. 2. Flowchart showing the different stages of the procedure used in this experimental investigation.

Table 1
Statistical parameters of Cr in agricultural soil (Ap) in Europe for the whole data set and the subset used in this study.

Data set	n	DL	Min	P10	P25	P50	P75	P90	Max	MAD	Mean	SD	IQR	Range
All data	2032	0.2	**<0.1**	5.7	11.3	**20.1**	32.2	47	**696**	10.2	27.3	37	20.8	696
Outlier-free data	1919	0.2	**<0.1**	5.5	10.7	**19.1**	29.7	40.2	**63.3**	9.4	21.3	13.4	19.1	63

Notes: All data, namely data sets without sample points, are in the excluded islands. Outlier-free data and statistically defined high outlier values are set without the islands. Min and Max: minimum and maximum values, respectively. P - percentiles. P50 is the median. MAD - median absolute deviation. DL – detection limit. SD - standard deviation. IQR - inter-quartile range. Bold font style emphasises the minimum, maximum and median values. Concentration values are given in units of mg/kg. See text for details.

ilmenite, and wolframite.

Within a sedimentary context, chromium occurs in primary detrital minerals such as chromite, ilmenite, and magnetite. Even in extensively weathered terrains, such as lateritic profiles, Cr levels can remain elevated (Delina et al., 2020). During weathering, Cr^{3+} mimics the behaviour of Fe^{3+} and Al^{3+} and tends to concentrate in secondary clay and oxide phases (Hseu et al., 2018). Chromium is not particularly mobile in the soil environment, with its movement regulated by pH, redox conditions, organic carbon content, and clay mineralogy (Berger and Frei, 2014; Hseu et al., 2018). At higher pH, Cr^{3+} readily co-precipitates with Fe^{3+} as insoluble $Cr(OH)_3$ (Albanese et al., 2015), and its adsorption onto clay particles is also pH-dependent — Cr^{3+} sorption increases with pH, while Cr^{6+} sorption diminishes (Albanese et al., 2015). Organic matter plays a crucial role by reducing toxic Cr^{6+} to the more stable Cr^{3+}, a process enhanced by increasing soil acidity (Kabata-Pendias and Pendias, 2001; Albanese et al., 2015). At soil pH values between 5 and 9, chromium predominantly exists in the reduced forms Cr^{3+}, $CrOH^{2+}$, and $Cr(OH)_2^{+}$. Typical natural soil Cr contents range from 10 to 50 mg/kg and can reach 350 mg/kg in agricultural settings (Ertani et al., 2017); the GEMAS agricultural soil samples show a range of 19.5 to 50.9 mg/kg, with anomalies exceeding 237 mg/kg (Albanese et al., 2015).

The present work aims to delineate and examine the continental-scale spatial distribution of Cr in European agricultural topsoil (0–20 cm depth) and to verify spatial data analysis techniques initially used for the Ni study (Jordan et al., 2018). Thus, current research builds on prior digital image processing work with Ni by extending the method to Cr, a metal with a similar geochemical behaviour. Unlike Ni, Cr poses challenges such as variable oxidation states and heterogeneous distribution, making its analysis more complex. Validating image-based quantification for Cr demonstrates the technique's adaptability and robustness, expanding its application to a broader range of elements. In this study, the methodology is further expanded to bivariate analysis by analysing hot Aqua Regia extractable (Cr_{AR}) and XRF (Cr_{XRF}) total Cr concentrations together, in addition to the analysis of Ni—Cr ratios (Fig. 2).

2. Materials and methods

Under the EuroGeoSurveys GEMAS project (Geochemical Mapping of Agricultural and Grazing Land Soil), a total of 2108 agricultural soil samples were collected from routinely tilled fields (Ap horizon, 0–20 cm depth), using a uniform 50 × 50 km grid system that averages one sample per 2500 km^2 (Reimann et al., 2014a, 2014b). The sampling adhered strictly to the guidelines established by the EuroGeoSurveys Geochemistry Working Group (2009). Complete documentation concerning sample processing, analytical protocols, and quality assurance practices is provided in earlier works (Reimann et al., 2009, 2011; Birke et al., 2014; Demetriades et al., 2014). Chromium (Cr) was determined by inductively coupled plasma mass spectrometry (ICP-MS) following digestion with hot aqua regia. At the 95 % confidence interval, the precision for Cr was estimated to be roughly ±6 %, with sources of variability partitioned into natural geochemical (98.9 %), sampling (0.4 %) and analytical variation (0.7 %) (Reimann et al., 2009; Demetriades et al., 2014). The total combined measurement uncertainty, based on an unbalanced variance design with three replicates per site, was calculated to be ±13.9 % at the 95 % confidence level (Ramsey, 1998; Ramsey et al., 2019).

Additionally, Cr concentrations were measured using wavelength-dispersive X-ray fluorescence spectroscopy (WD-XRFS), employing PANalytical PW2400 and AXIOS instruments fitted with Cr and Rh anode X-ray tubes (Reimann et al., 2011), respectively. The reported precision for this method is approximately ±3 % at the 95 % confidence level, with analysis of variance components partitioned into natural geochemical (98.0 %), sampling (1.0 %), and analytical (1.0 %) contributions (Reimann et al., 2011; Demetriades et al., 2014). The overall measurement uncertainty is ±14.5 % at the 95 % confidence level (Ramsey, 1998; Ramsey et al., 2019).

For the present investigation, 2032 of the original 2108 samples were retained after applying spatial filtering criteria described by Jordan et al. (2018) (see Table 1 and Figs. 3 and 4). The statistical treatment of the data included descriptive statistics such as minimum, quartiles, median, maximum, and median absolute deviation (MAD). Anomalous Cr values were identified using Tukey's inner-fence rule for outlier detection (Tukey, 1977) (Fig. 4B). Concentrations below the 0.2 mg/kg detection limit were replaced with half the limit value to facilitate further statistical processing and map plotting. Chromium levels were also assessed across various bedrock types using box-and-whisker plots (Kürzl, 1988), sorted in ascending order by median values (Figs. 4B). Since the core objective was to evaluate broad regional distribution trends, 113 extreme Cr outliers (≥63.5 mg/kg) were removed, resulting in a final data set of 1919 data points for interpolation and spatial evaluation.

As a comparison, scatter-plots were plotted on a log-log scale (base 10) depicting Cr_{AR} vs Cr_{XRF} concentrations, including outliers ($n = 2032$ samples) and outlier-free data set ($n = 1919$) (AR: Aqua Regia; XRF: X-ray Fluorescence). As expected, both plots display higher concentrations for total XRF than AR-derived Cr data (Fig. 5). The trend is linear on a log-log scale (base 10), indicating a power-law relationship (~1) between the two data sets. This scale independence reinforces our concept that Cr_{AR} is adequate to capture the large-scale spatial patterns in Cr concentrations with higher accuracy. The trend is stable ($R^2 \approx 0.8$), and there appears to be no larger variability at higher or lower concentrations (i.e., no heteroscedasticity) (Fig. 5). Thus, this study uses the hot aqua regia digestion (ICP-MS) data unless otherwise specified.

The Cr interpolation map was generated using Triangular Irregular Network (TIN) interpolation methods (Guibas and Stolfi, 1985; Davis, 2011), resulting in a continuous 10 × 10 km raster surface. The output was processed from basic univariate visualisation to advanced spatial feature extraction utilising digital tools such as edge detection, segmentation, and GIS-driven multivariate analysis (ESRI, 2011). A smoothing filter — using moving average with a 9 × 9 window (90 × 90 km) — was applied to highlight macro-scale geochemical trends (Gonzalez and Woods, 1993).

Fig. 6A shows a Cr concentration map utilising Exploratory Data Analysis symbols (Tarvainen et al., 2022), and Fig. 6B a contour map derived from the smoothed interpolation surface without outliers displaying abrupt Cr concentration changes (e.g., 12 mg/kg breakpoint in Fig. 3A). Visual lineament analysis was facilitated through shaded relief rendering; digital cross-section profiles were constructed to study directional variation across and along key geospatial anomalies (Fig. 6 and Appendix SM1). Terrain Ruggedness Index (TRI) analysis was

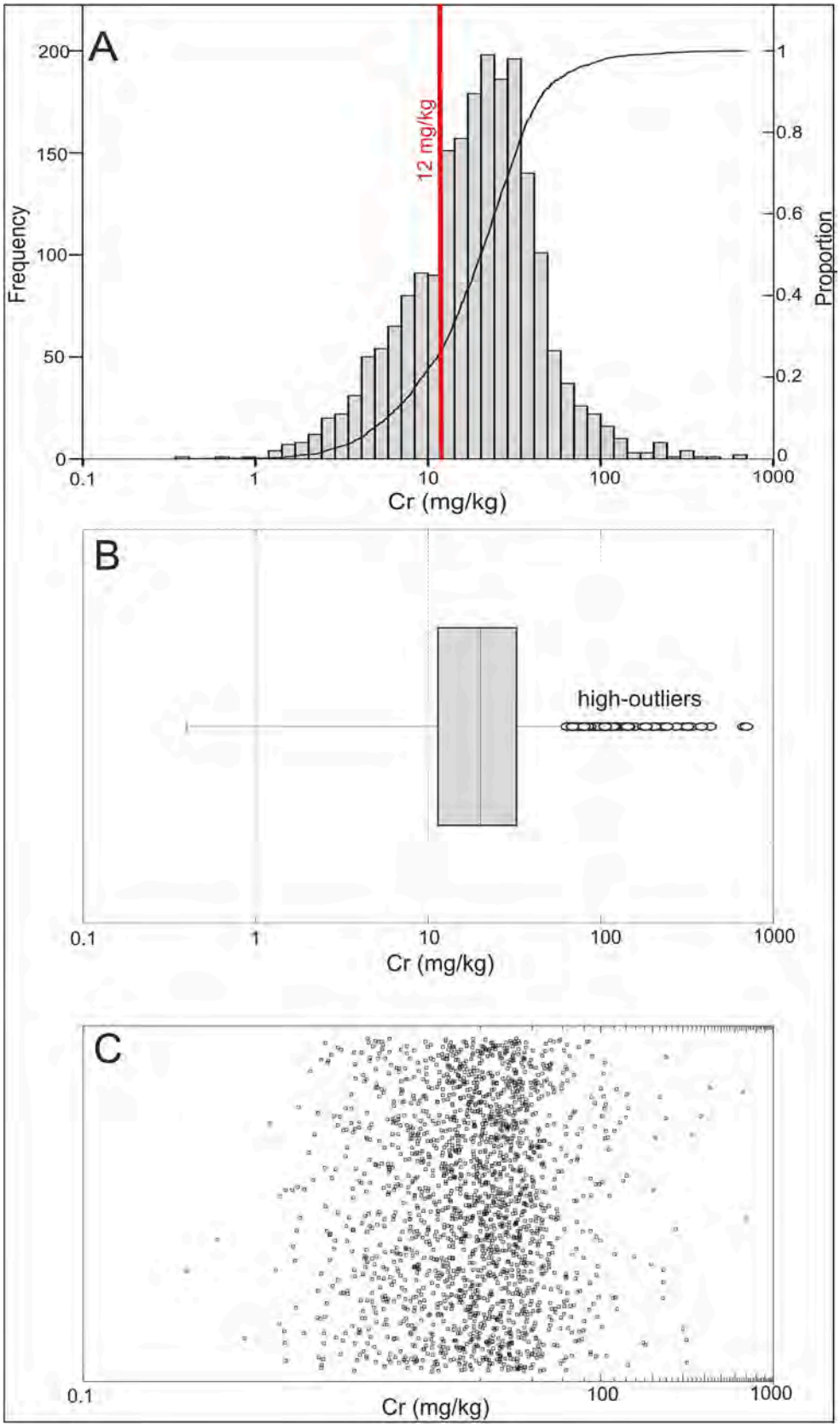

Fig. 3. Statistical univariate distribution of hot aqua regia Cr concentrations in agricultural (Ap) soil samples. (A) Empirical histogram with the cumulative frequency distribution curve; note the distinct break at 12 mg/kg. (B) Boxplot showing the univariate statistical distribution and high-outliers. (C) Two-dimensional scatterplot. Note the $\log_{10}$-scale of the X-axis in all plots. (For interpretation of the references to colour in this figure legend, the reader is referred to the web version of this article.)

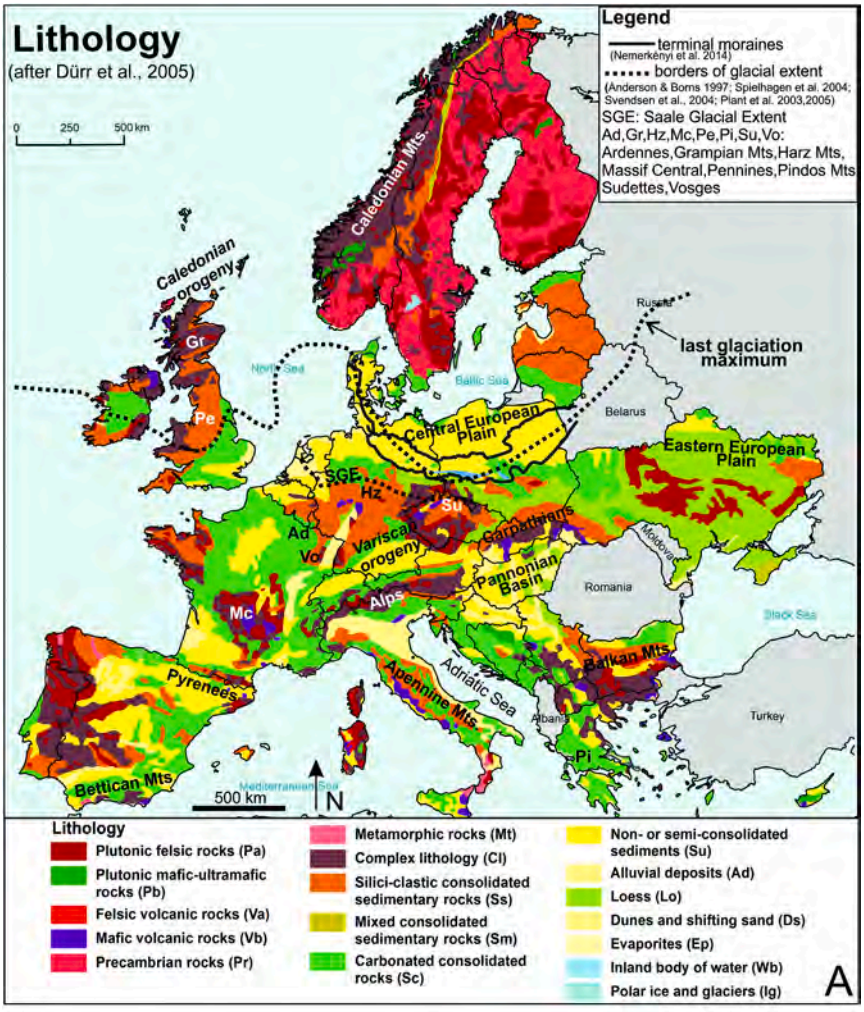

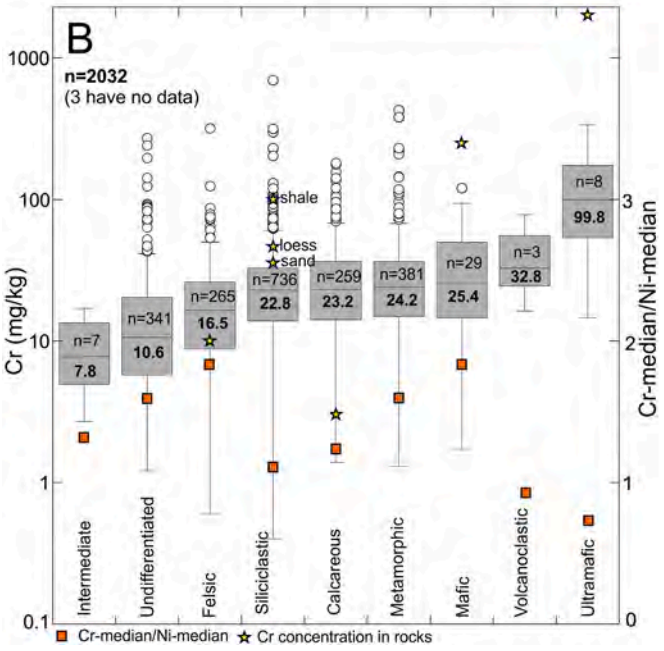

(caption on next page)

Fig. 4. (A) Lithology map of Europe (modified after Dürr et al., 2005). (B) Box-and-whisker plots of hot aqua regia extractable Cr concentrations in agricultural (Ap) soil samples calculated for different bedrock parent materials arranged in an increasing order of median values; bold numbers in the boxes indicate the median value of the corresponding group; n denotes the number of samples in the corresponding group. Note that volcanoclastic rocks have only 3 samples. The average Cr concentration in various rock types (Reimann and de Caritat, 1998) is also shown (star symbol with yellow centre). The median ratios of Cr and Ni in topsoil, calculated for various bedrock parent materials, are also displayed (square symbol with red centre), corresponding to the y-axis on the right. (For interpretation of the references to colour in this figure legend, the reader is referred to the web version of this article). (For interpretation of the references to colour in this figure legend, the reader is referred to the web version of this article.)

performed following the method of Riley and Degloria (1999) to reveal Cr variability patterns (Fig. 8), and specific terrain points — local peaks, pits, flats, and slope discontinuities — were used to distinguish zones of anomaly, constancy, or abrupt spatial transition.

Directional empirical variograms were employed to assess anisotropy in Cr spatial patterns (Cressie, 1993; Gosar et al., 2016) (see Fig. 9 and Appendix SM2). A residual map was generated by subtracting the outlier-free smoothed TIN-interpolated Cr concentration (regional trend surface) from the observed Cr values at the sampling points, aiming to detect unexplained local variations (Fig. 10). The residual values at sampling points were normalised with respect to the standard deviation before their interpolation to enhance subtle variations, which are then compared with lithology, known Cr-mineralisation sites, and other geological features. To validate the spatial model results, GIS overlays were used to compare the interpolated Cr spatial distribution with geological maps of parent materials (Hartwich et al., 2005), lithology (Dürr et al., 2005), and Quaternary glacial extent (Anderson and Borns Jr, 1997; Plant et al., 2003, 2005; Spielhagen et al., 2004; Svendsen et al., 2004).

The interpolated geochemical map of Cr concentrations is a raster map of a continuous surface of a bivariate function, similar to the digital terrain model (Li et al., 2004) of the topographic surface. Thus, the geochemical map can be examined using digital terrain analysis methods. The gradient magnitude ('slope') and direction ('aspect') were calculated for each raster cell to capture the rate of Cr concentration and its direction, respectively (see Figs. 11 and 12). Zones with steep gradients aligned with directional trends may point to underlying geological structures (Jordan et al., 2018). Profile curvature, the second derivative in gradient direction, was used to flag locations of sharp change and to delineate convex and concave regions (Fig. 13), which, when aligned, may reflect tectonically influenced distributions; it also reflects the N-S discontinuity between continental glaciated environments in the north and non-glacial soil to the south. Sub-populations of Cr concentrations were established using Jenks natural break histogram segmentation (Abdaal et al., 2013), which were visualised as homogenous zones in classified Cr maps (Figs. 11–13). As shown in the GEMAS Atlas, 'a north-south division' along an east-west alignment in Cr levels separates lower northern from higher southern European concentrations, coinciding with the maximum limit of the last continental glaciation. High Cr clusters in the Balkans and northern Italy are mainly linked to mafic-ultramafic lithologies and regional mineralisation zones.

The limitation of the spatial analysis methodology is defined by standard digital image processing techniques, most prominently, the sampling frequency (minimum distance of sampling points) and the resolution of the interpolated grid, which define the smallest feature that can be identified.

This work also involved a comparative analysis of Cr and Ni concentrations, given their similar geochemical behaviour and earlier spatial modelling of Ni (Jordan et al., 2018). Their relationship was explored using bivariate molar concentration regression (Fig. 14), while their spatial distributions were compared by calculating the Cr/Ni ratio at each grid node from the smoothed, interpolated data sets (Fig. 15).

To further explore the behaviour of Cr in the studied secondary topsoil environment, the ratio of Cr concentrations measured by hot aqua regia and XRF was also calculated (Figs. 15 and 16). The comparison between hot aqua regia-extractable Cr and total Cr, as determined by XRF, offers valuable insights into the relative lability of Cr in soil. Aqua regia predominantly extracts the acid-soluble, reducible, and oxidisable fractions of Cr. The behaviour of Cr is governed by organic matter complexation and adsorption by clay minerals. Thus, depending on pH and Eh in the secondary environment, phases are readily dissolved by hot aqua regia (Kabata-Pendias and Pendias, 2001). However, aqua regia does not capture the entire geochemically labile pool. Conversely, XRF measures total Cr, including highly stable mineral phases such as spinels and chromite; therefore, the Cr_{AR}/Cr_{XRF} ratio is indicative of mineralogical composition. In addition, by assuming that XRF delivers true total Cr concentrations in the studied agricultural soil samples, the proportion of aqua regia extractable Cr (Cr_{AR}) to the XRF-measured total Cr content (Cr_{XRF}) may provide an estimation of the extractability of Cr in the studied European agricultural topsoil. However, neither of the methods differentiates between Cr(III) and the more mobile and toxic Cr(VI) species (Saha et al., 2011).

All spatial modelling and map plotting were conducted using Golden Software's Surfer™ (v25), ILWIS 3.8, and Esri's ArcGIS® 10.8 platforms. Graphical visualisations, including scatter plots, were plotted with Grapher™ version 25 (Golden Software).

3. Results

3.1. Statistical analysis

Based on the histogram and cumulative distribution plot (Fig. 3), the hot aqua regia extractable Cr data set ($n = 2032$) displays a unimodal, right-skewed distribution, with 113 high outliers (≥63.5 mg/kg) identified using Tukey's inner-fence method (Tukey, 1977). Chromium levels range from <0.2 (0.1) to 696 mg/kg, with a median of 20.1 mg/kg and a median absolute deviation (MAD) of 10.2 mg/kg (Table 1). A distinct breakpoint at 12 mg/kg is observed in the frequency histogram, which was subsequently used to categorise Cr concentrations (Figs. 3A and 4B).

Out of the 2032 sampling points, 2029 were classified into eight primary bedrock types according to the lithology map shown in Fig. 4A. The associated Cr concentrations for each bedrock type were visualised using box-and-whisker plots for comparative analysis (Fig. 4B). It is noted that 3 samples have no lithological information, and 341 samples were taken from areas over undifferentiated parent materials (e.g., alluvial, diluvial or glacial drift sediments). Fig. 4B demonstrates that ultramafic rocks have the highest median Cr concentration value (99.8 mg/kg, $n = 8$), followed by volcanoclastic (32.8 mg/kg, $n = 3$), mafic (25.4 mg/kg, $n = 29$), metamorphic (24.2 mg/kg, $n = 381$), carbonate (23.2 mg/kg, $n = 259$), siliciclastic (22.8 mg/kg, $n = 736$), felsic (16.5 mg/kg, $n = 265$), undifferentiated (10.6 mg/kg, $n = 341$) and intermediate (7.8 mg/kg, n = 7) rocks. The Mann-Whitney test (Mann and Whitney, 1947) indicates that four distinct groups can be identified based on the similarity of median values at the 95 % confidence level. The first group comprises agricultural soil samples overlying undifferentiated and intermediate rocks; the second group includes only soil developed on felsic parent materials; the third group consists of soil over siliciclastic, carbonate, metamorphic, and mafic rocks, while the fourth group includes only those over ultramafic rocks. Due to the limited number of samples (n = 3), topsoil over volcanoclastic rocks could not be statistically evaluated using the Mann-Whitney test. The Cr and Ni medians, calculated for the same parent materials, were also compared based on their similar geochemistry. The Cr medians are generally higher (Cr-median/Ni-median > 1), except in topsoil over volcanoclastic and ultramafic parent materials, where the Cr-median and Ni-median ratio is below one (Fig. 4B).

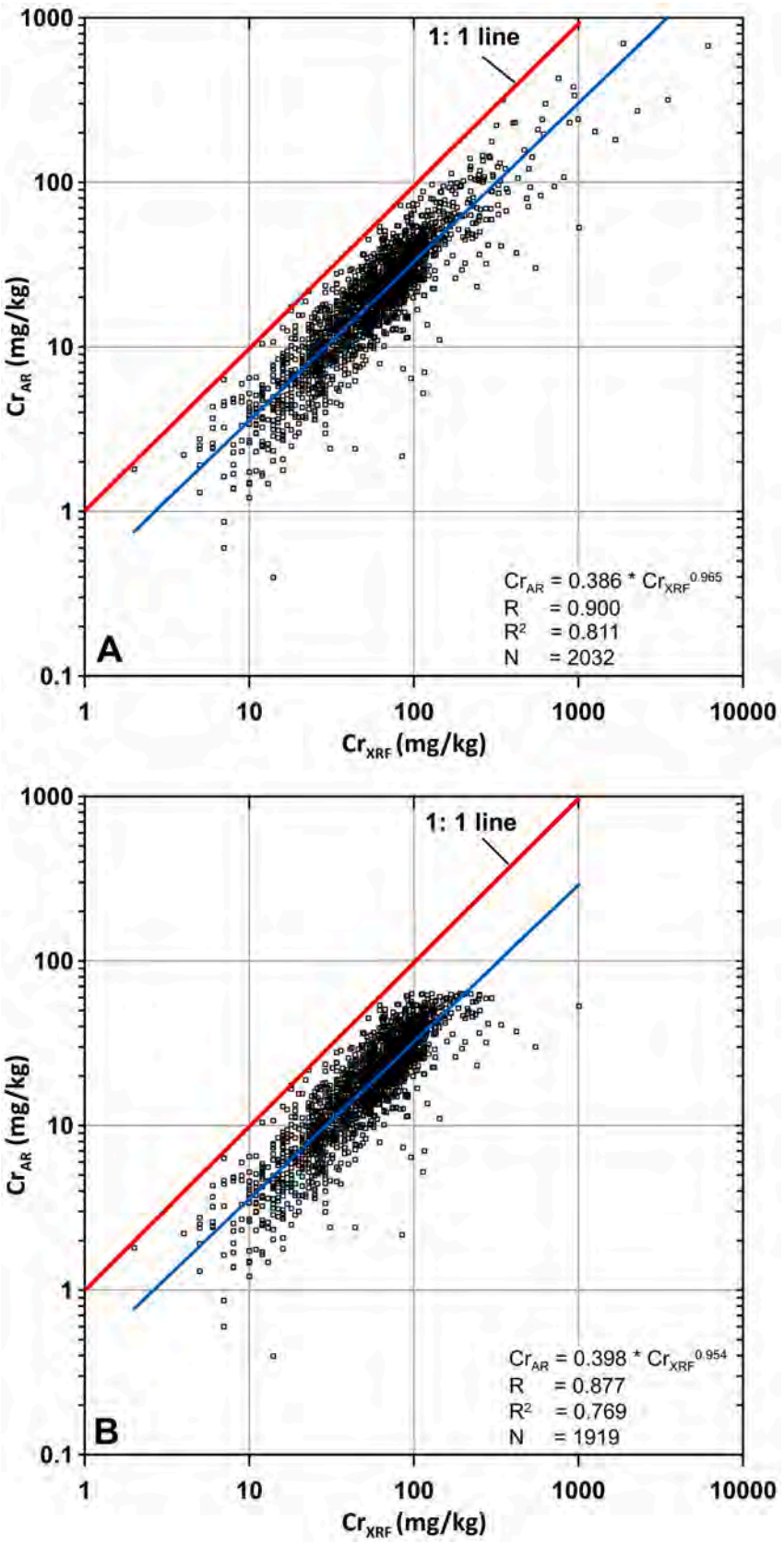

Fig. 5. Bivariate scatter plots of Cr determined by XRF and hot Aqua Regia extraction. (A) The whole data set ($n = 2032$) and (B) The outlier-free data set ($n = 1919$). Note the blue colour line and the corresponding high linear correlation coefficients ($R_{(A)} = 0.900$ and $R_{(B)} = 0.877$) between them. The axes are in the $\log_{10}$-scale. (For interpretation of the references to colour in this figure legend, the reader is referred to the web version of this article). (For interpretation of the references to colour in this figure legend, the reader is referred to the web version of this article.)

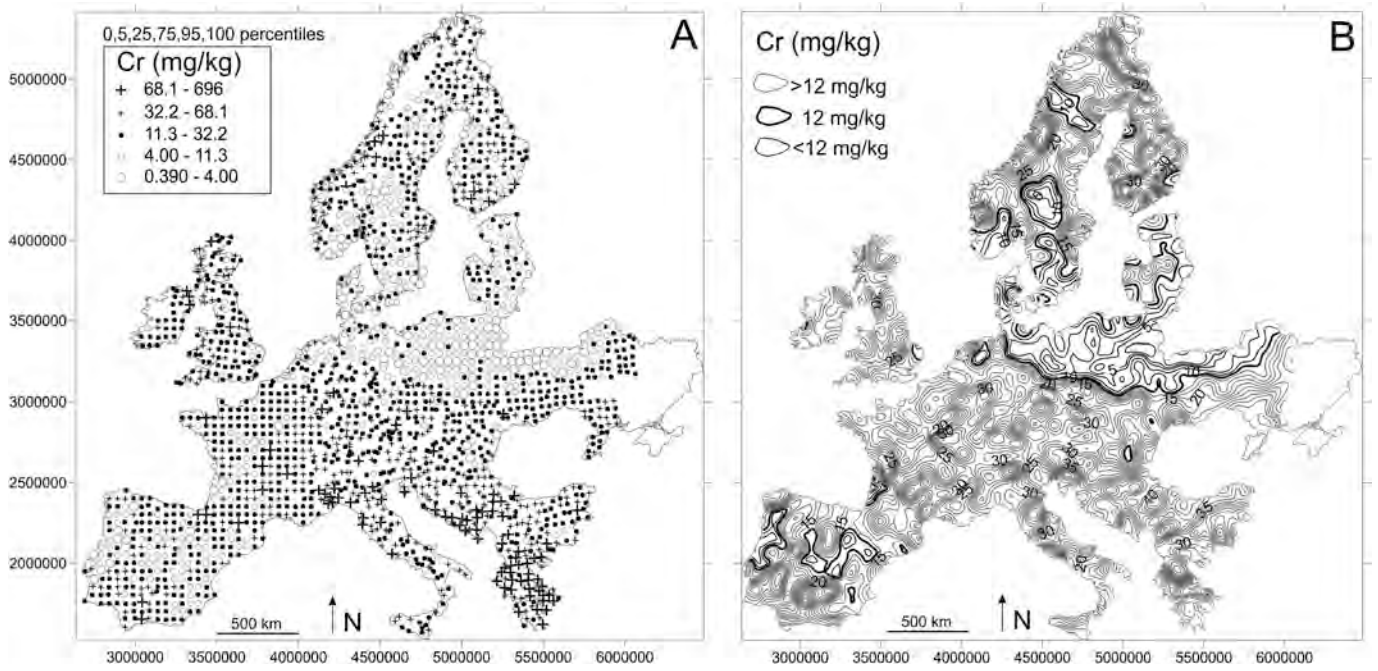

Fig. 6. (A) Chromium concentration map based on percentile symbols (n = 2032). (B) Classified Cr-contour map based on the breakpoint at 12 mg/kg in the frequency histogram (see Fig. 3A). Note that low Cr concentrations are located along the *E*-W zone of the last continental glacial maximum and terminal moraines (see Fig. 4A). The highest Cr concentrations are observed in the Balkan Peninsula and northern Italy where mafic and ultramafic rocks outcrop, as well as sediments derived from them.

3.2. Mapping and spatial analysis

The Cr concentration map, categorised by percentiles, shows that most low-value samples (5th percentile: <4.0 mg/kg) are concentrated within an east–west trending zone in the northern part of the Central European mainland (Fig. 6A and B). This area roughly corresponds to the Central European Plain and is bounded to the south by the extent of the last continental glaciation and its associated terminal moraines (Fig. 4A). The distinct break at 12 mg/kg of Cr in the frequency histogram (Fig. 3A) also coincides with the *E*-W trending last glaciation maximum (Fig. 6B). A NE-SW oriented, linear low Cr zone lies across France between the Aquitaine and Paris Basins. A few roughly N-S trending low Cr zones occur in the Iberian Peninsula, while low Cr concentrations mainly characterise Portugal. More randomly distributed low Cr areas occur in Fennoscandia, as well as in the southern regions of Norway and Sweden (Fig. 6A). In contrast, elevated Cr concentrations (>68.1 mg/kg, 95th percentile) are predominantly clustered in the Balkan Peninsula and northern Italy, particularly within the Alps and Apennine Mountains. These high values are attributed to the occurrence of mafic and ultramafic rock outcrops and the sediments derived from them (Figs. 4A, 6A and 6B).

The shaded relief model of the smoothed TIN-interpolated raster map highlights several regional linear patterns of locally elevated Cr concentrations, oriented in a NE–SW direction across the western part of continental Europe (Fig. 7A). In contrast, the EN*E*-WSW direction prevails in the south-eastern part. These zones of elevated Cr concentrations are characterised by aligned local maxima points. The sub-parallel NE–SW-oriented bands extend for hundreds of kilometres, with a few of them aligning with the strike of major mountain chains, such as the Alps and the Carpathians. Local minima zones subdivide and follow the trend of high Cr zones in continental Europe, apart from some N-S trending minima zones in the Iberian Peninsula. Another notable feature is the roughly E-W oriented, continuous undulating line formed by several local Cr minimum points along the southern border of the Central European Plain, running sub-parallel to the southern boundary of the maximum extent of the last continental glaciation (Figs. 4A, 6A, B and 7A).

Fig. 7B shows the positions of cross-sections of Cr concentrations made perpendicular and parallel to the main spatial features. These cross-sections are displayed in profiles (1–5), where distinct slope breaks are indicated by thick red lines and trend envelopes are shown with orange dashed lines. The NW-SE oriented cross-sections, as shown in Profiles 1 and 2 in Fig. 7C, calculated from the smoothed TIN Cr concentration raster map, running across the centre of the study area, transect the elongated NE-SW zones and display abrupt changes and asymmetries in Cr concentrations. The substantial extent of the low Cr area in the Pannonian Basin is well visible (Fig. 7, Profile 2). The N-S trending Profile 3 reveals a distinct break at the southern limit of the last glacial maximum and a continuous increase of Cr concentration in a southward direction; zones of high Cr concentration appear as peaks over prominent mountain ranges, such as the Ardennes and the Balkan Mountains. These peaks exhibit asymmetric shapes and are bordered by pronounced slope breaks, where Cr concentrations rise sharply. Profile 4 reveals a distinct break at the northern edge of Norland and a decreasing trend of Cr concentrations southward from the Norland maximum zone. The NE-SW trending Profile 5 also captured the distinct break at the southern limit of the last glacial maximum, from where there is a sudden increase in Cr concentrations toward the Vosges.

The lack of homogeneity in the spatial variation of Cr was overcome by log-transforming the Cr values prior to the calculation of the Terrain Ruggedness Index (TRI). The derived TRI map was further refined for visual interpretation through post-processing with a 110 × 110 km moving average smooth (Fig. 8A and B). The most striking feature is the broad region of low Cr variability in the northern part of the Central European mainland, with its boundary aligning with the southern extent of the last glacial maximum. North of the Alps, another hundreds of kilometres long, *E*-W trending low variability zone can be observed from the Massif Central to the Pannonian Basin, which seems to follow the trend of the Alpine thrust front (Fig. 8). Low variability zones (<20.7 mg/kg TRI) also occur in the north-western part of continental Europe, in the Iberian Peninsula, in the southern parts of Ireland and the Scandinavian Peninsula, and the Pannonian Basin in central-eastern Europe.

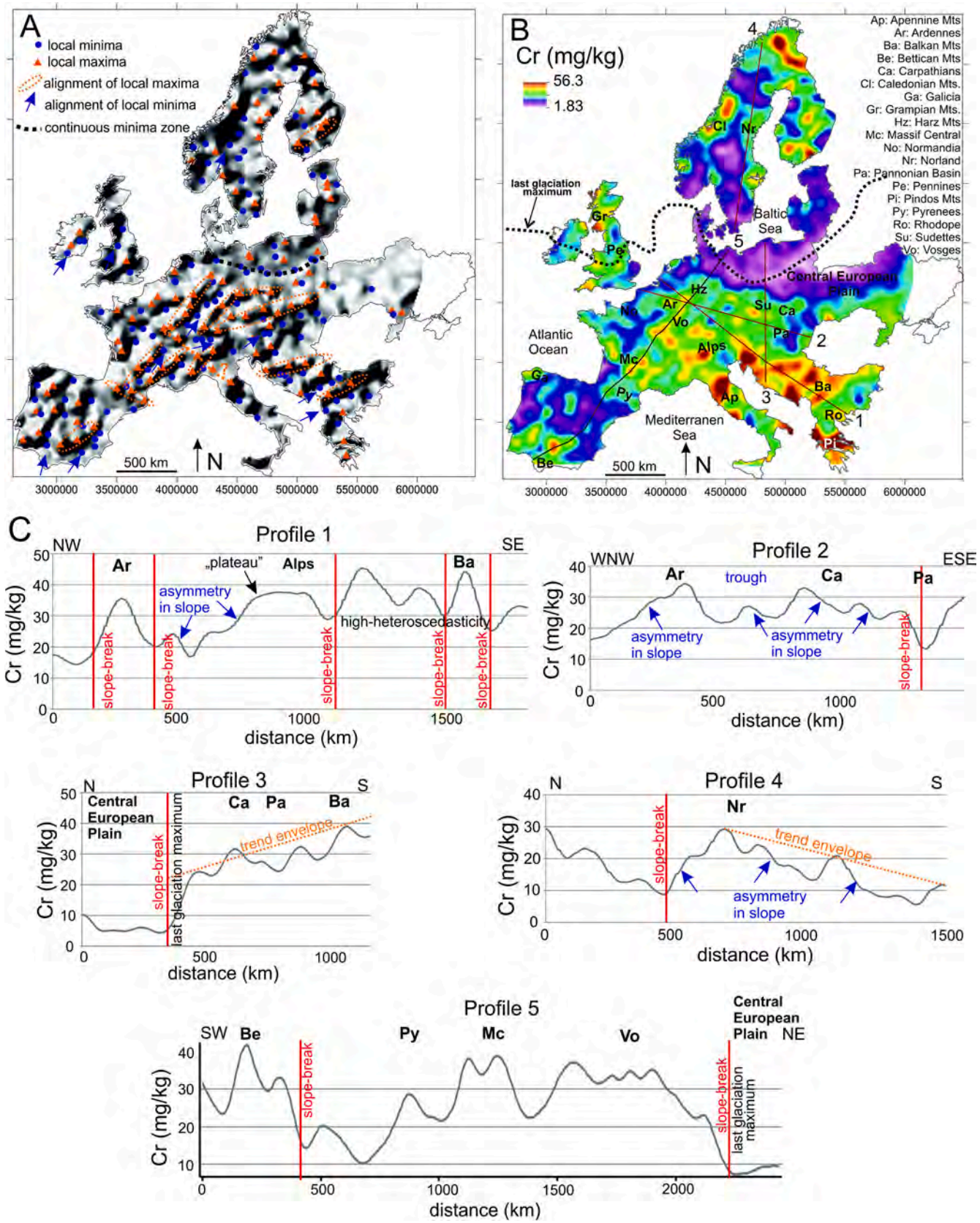

Fig. 7. (A) Shaded relief map of the outlier-free Cr data overlain by the local minima and maxima points; note their dominating NE-SW and ENE-WSW alignments emphasised by blue arrows and orange dashed ellipsoids. (B) TIN-interpolated Cr concentrations map with black lines of cross-sections shown in (C): Cross-sections of Cr concentrations made perpendicular and parallel to the main spatial features; distinct slope breaks are shown with thick red lines and trend envelopes with orange dashed lines. Locations of cross-sections are shown in Fig. 7B. (For interpretation of the references to colour in this figure legend, the reader is referred to the web version of this article). (For interpretation of the references to colour in this figure legend, the reader is referred to the web version of this article.)

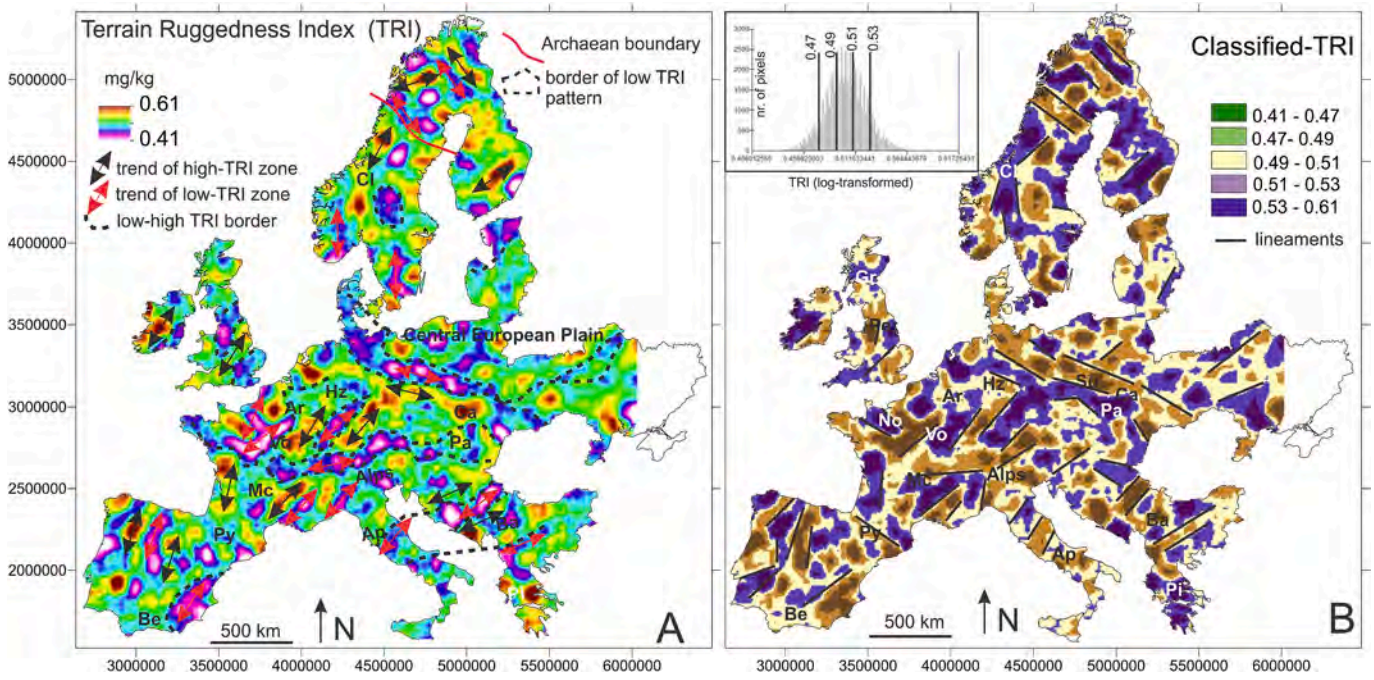

Fig. 8. (A) Terrain Ruggedness Index (TRI) map of outlier-free $\log_{10}$ transformed Cr values; note the prevailing low variability zones in the northern and north-western parts of continental Europe; also notice the roughly E-W border along the Central European Plain, which separates low and high Cr variability zones. (B) Classified TRI map of $\log_{10}$ transformed Cr values, based on histogram slicing. For abbreviated names, refer to the legend of Fig. 7B. (For interpretation of the references to colour in this figure legend, the reader is referred to the web version of this article).

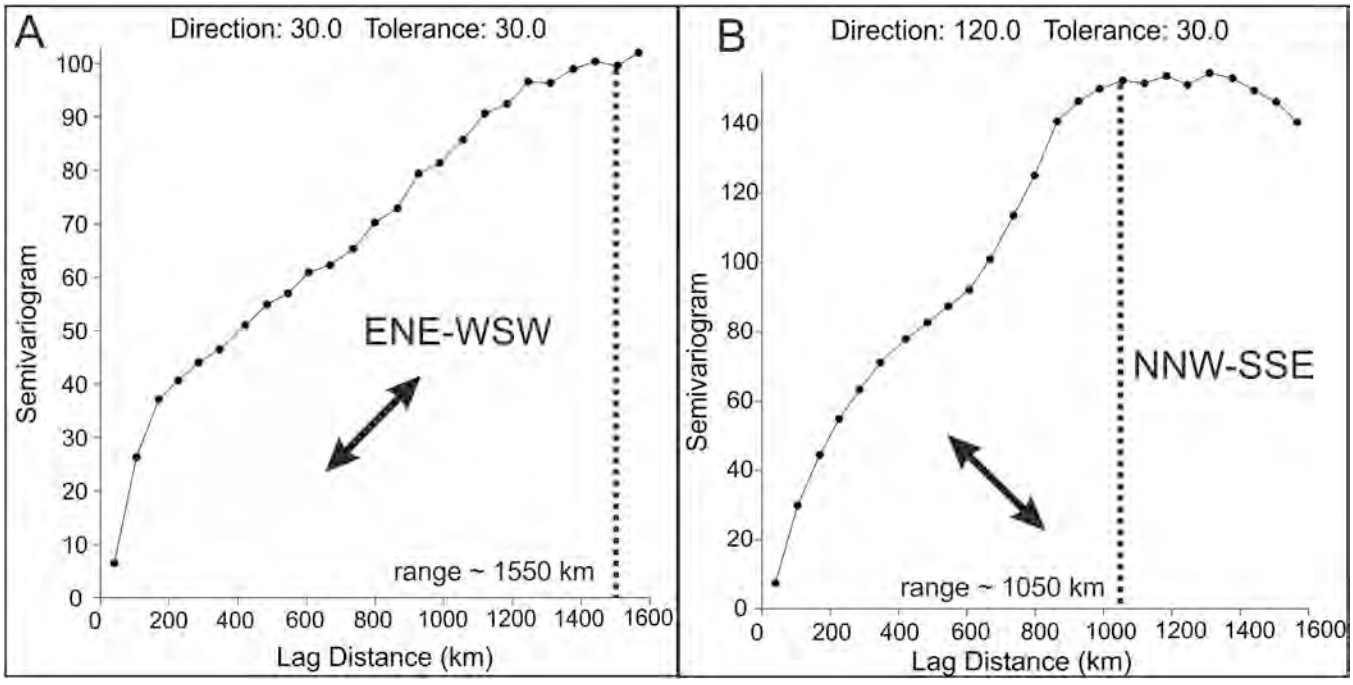

Fig. 9. Directional semi-variograms of Cr in ENE-WSW (A) and NNW-SSE (B) directions. Note the longer range of influence in the ENE-WSW direction. The averaged semi-variogram values are displayed on the y-axis.

The abundance of NNE-SSW striking alternation of low and high variability zones spanning from the Iberian Peninsula to the Pannonian Basin is also remarkable. Similar trends are visible in the Caledonian Mts, Apennine Mts, Balkan Peninsula and Great Britain. A clear NW-SE line in northern Scandinavia coincides with the contact between Archaean and Palaeo-Proterozoic rocks, known as the Archaean Boundary (Fig. 8). Interestingly, the trend of low and high variability zones changes to NW-SE north of the Archaean boundary. High variability zones (>0.53 mg/kg TRI) are observed in the Balkan Peninsula, the Pindos Mts (Hellenic Republic), the Baetic Mts (Spain), and some parts of the Caledonian Mts and Finland. The separation of high- and low-variability zones is often sharp and linear on the classified TRI map (Fig. 8B).

The directional semi-variograms show a pronounced ENE-WSW

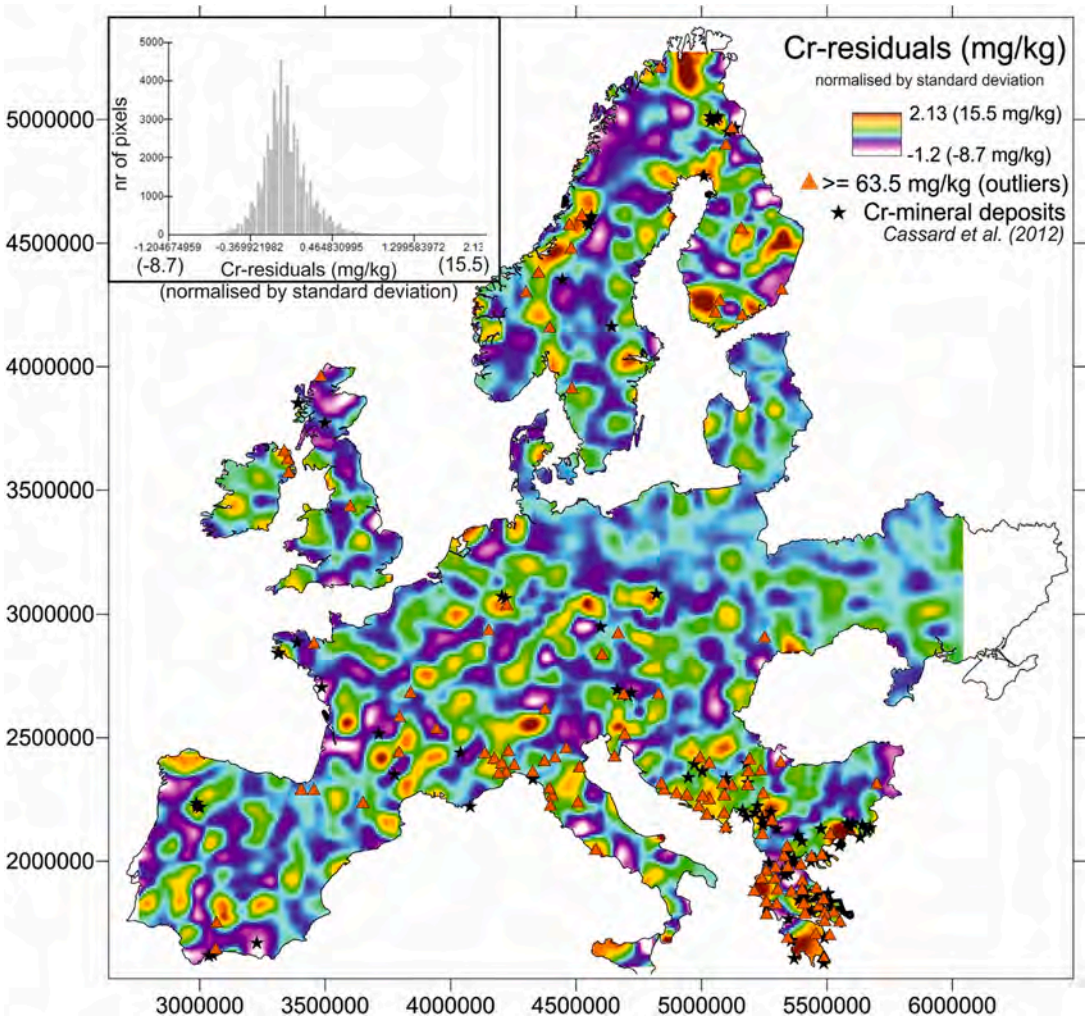

Fig. 10. Chromium residual map. To increase visibility and interpretability, the $\log_{10}$ transformed residuals were normalised with respect to the standard deviation. The histogram of normalised and log-transformed Cr residuals is shown in the inset. In the legend, the untransformed residual values (mg/kg) are given in brackets. Occurrences of Cr mineral deposits and mineralisation are from Cassard et al. (2012, 2015). (For interpretation of the references to colour in this figure legend, the reader is referred to the web version of this article).

trending anisotropy in the spatial distribution of Cr concentrations, aligned with the pattern of local maxima and minima points (Figs. 7A and 9A). The range in the EN*E*-WSW direction is approximately 1550 km, compared to only 1050 km in the perpendicular NNW-SSE direction (Fig. 9B). The same anisotropy was found in the spatial distribution of Ni values (Jordan et al., 2018).

The calculated residual Cr map reveals the local deviation of Cr concentrations from the large-scale spatial trend modelled with the smoothed TIN surface. Positive deviations indicate that the Cr concentration at sampling sites is higher than the modelled Cr concentration (Fig. 10). The residual map highlights the highest positive deviation zones in the Balkan Peninsula and northern Italy corresponding to ophiolite zones with known Cr-mineral occurrences and deposits and statistically defined high Cr outliers. A few scattered positive deviations are oriented in the NE-SW direction across France, and parallel to the Caledonian Mts. The spatial pattern of negative deviation zones is more random, except for a few NE-SW trending features across France between the Aquitaine and Paris Basins. The smallest deviations can be observed in the northern part of continental Europe, particularly over glacial sediments (e.g., Central European Plain), where the Cr concentration is low.

The classified gradient magnitude (in percentage slope) map illustrates the changes in topsoil Cr concentrations along the direction of the gradient vector (direction of maximum change at a point). High Cr values signify a notable change over a given unit of distance (Fig. 11); Ni displays similar features (Jordan et al., 2018). The areas with the highest gradient magnitudes of Cr exhibit an elongated shape, oriented primarily in the NE-SW direction. An E-W-oriented high gradient magnitude zone marks the southern boundary of the Central European Plain, which roughly coincides with the boundary of the last glacial maximum. A few NW-SE trending high-gradient areas are observable in the southern part of the Balkan Peninsula and the northern part of Scotland and Finland.

The lowest Cr gradient magnitudes occur over the Central European Plain, and a remarkable ENE-WSW trending, continuous low-gradient zone extends from southern Germany to the Pannonian Basin. A few NW-SE low-gradient zones are also discernible in the northern Iberian and Scandinavian Peninsulas (Fig. 11). These low-gradient regions likely reflect areas of geochemical homogeneity, influenced by stable tectonic settings, extensive sedimentary cover, or glacial processes that limit the variability of chromium concentrations across these landscapes.

The classified gradient direction (aspect) maps, overlaid with local Cr minima and maxima points, are presented in Fig. 12A. Sharp edges acting as lineaments between areas with homogeneous gradient directions of Cr values are emphasised in Fig. 12B. The classified gradient direction (aspect) maps overlain by the local Cr minima and maxima

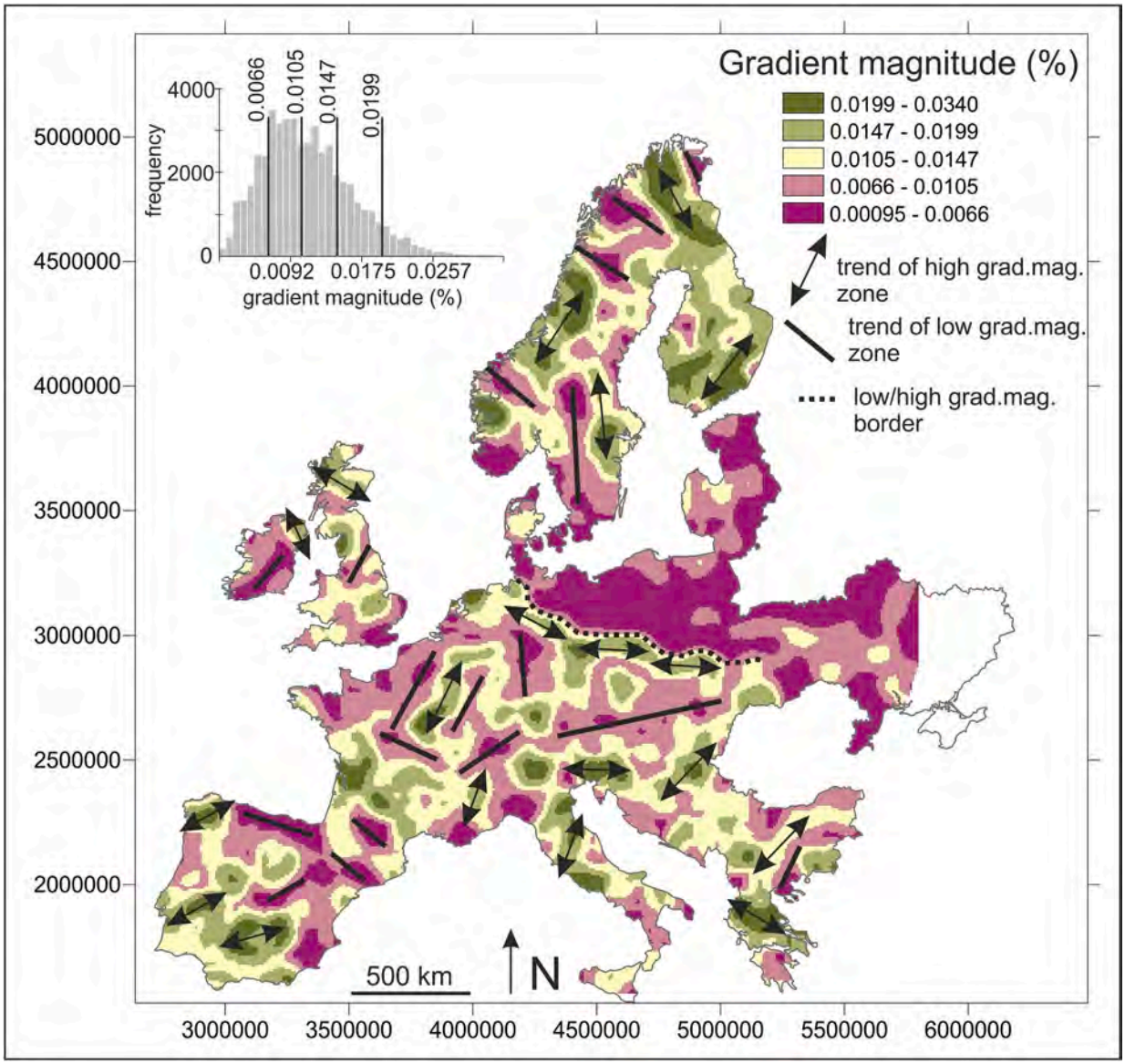

Fig. 11. Classified gradient map calculated from the smoothed TIN Cr concentration map. The map reveals the NE-SW, NW-SE, and E-W orientations of elongated linear features (emphasised by black arrows and lines), as well as the continuous border between high- and low-gradient zones in northern Central Europe (indicated by a black dotted line), which coincides with the southern limit of the last continental glaciation. Note the NE-SW trending long, low-gradient zone in the middle of Europe. Also, note the abundance of NW-SE trending low-gradient zones in the northern Scandinavian Peninsula. The histogram displays the classes based on natural breakpoints. (For interpretation of the references to colour in this figure legend, the reader is referred to the web version of this article).

points are shown in Fig. 12A. The sharp edges as lineaments between areas of homogeneous gradient direction of Cr values are emphasised in Fig. 12B. The histogram of the gradient direction, ranging from 0° to 360°, exhibits significant multi-modality, indicating peaks where pixels are facing in the same direction (Fig. 12C). The classified gradient direction Cr map is characterised by cross-cutting zones oriented ENE-WSW and NE-SW. These zones extend for hundreds of kilometres and are delineated by sharp linear edges (Fig. 12B). These features terminate at an E-W oriented broad, homogeneous, northward facing zone extending from the English Channel to the Eastern European Plain, the southern border of which is marked by the alignment of local maxima points, while its northern border is characterised by local minima points of the last glaciation maximum extent (Fig. 12A). The north-south digital cross-section through this zone also reveals a decrease in Cr concentrations as it extends northward (Profile 3 in Fig. 7C). At the same time, N-S oriented long features prevail in the whole Iberian and the western part of the Scandinavian Peninsula. A few noticeable NW-SE-oriented long spatial features were also identified across France, particularly near the southern limit of the Central European Plain (Fig. 12B). The rose diagram of the lineaments (Fig. 12D), digitised from Fig. 12B, illustrates the four primary directional trends, namely NW-SE, N-S, NE-SW, and ENE-WSW.

The second derivative of Cr concentrations, calculated along the gradient direction, is known as the profile curvature, which indicates changes in gradient magnitude (slope), such as slope breaks (Fig. 13). The profile curvature map is classified based on the sliced histogram of the outlier-free data set. In this figure, the main linear zones in Cr concentrations, oriented ENE-WSW and NE-SW, stand out as distinct features, displaying many high negative (convex; solid black lines) and positive (concave; dashed black lines) curvature values across continental Europe. These sub-parallel features end abruptly at a wavy east–west slope break (heavy dotted line) in northern Central Europe, extending for hundreds of kilometres.

It is interesting to note another E-W-oriented, long positive (concave)

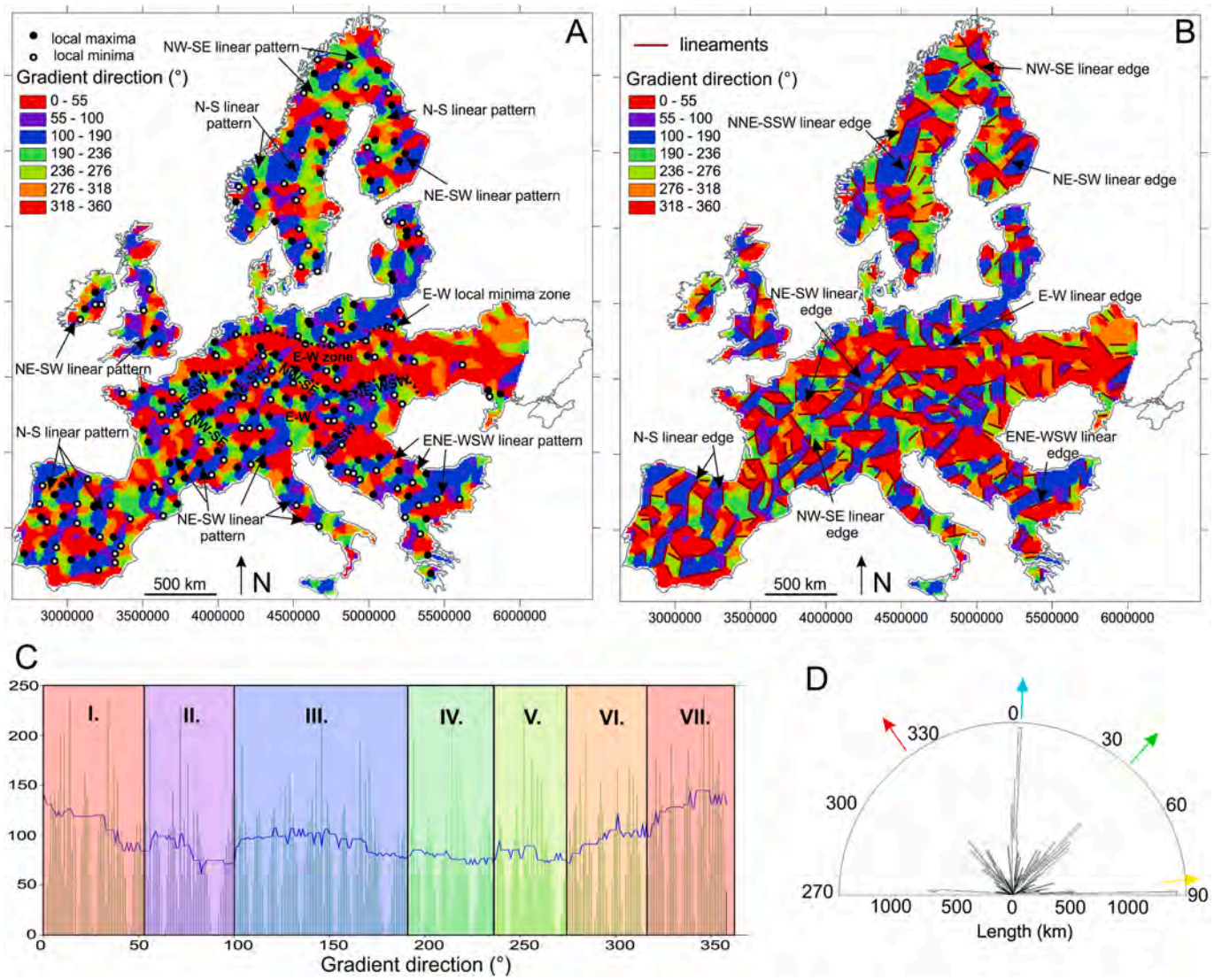

Fig. 12. (A) Classified gradient direction map overlain by the local minima and maxima (extreme) points; note the coincidence of the aligning extreme points with the prominent linear boundaries. (B) Classified gradient direction map overlain by lineaments digitised from this map (black lines). (C) Frequency distribution of gradient direction smoothed by 5 × 5 5RSSH median filter developed by Tukey (1977) (blue line); the classes were identified using histogram-slicing based on the natural breakpoints. (D) Length-based direction distribution of lineaments shown in Fig. 12B (black lines); note the 4 major orientations that correspond to the main linear features. (For interpretation of the references to colour in this figure legend, the reader is referred to the web version of this article). (For interpretation of the references to colour in this figure legend, the reader is referred to the web version of this article.)

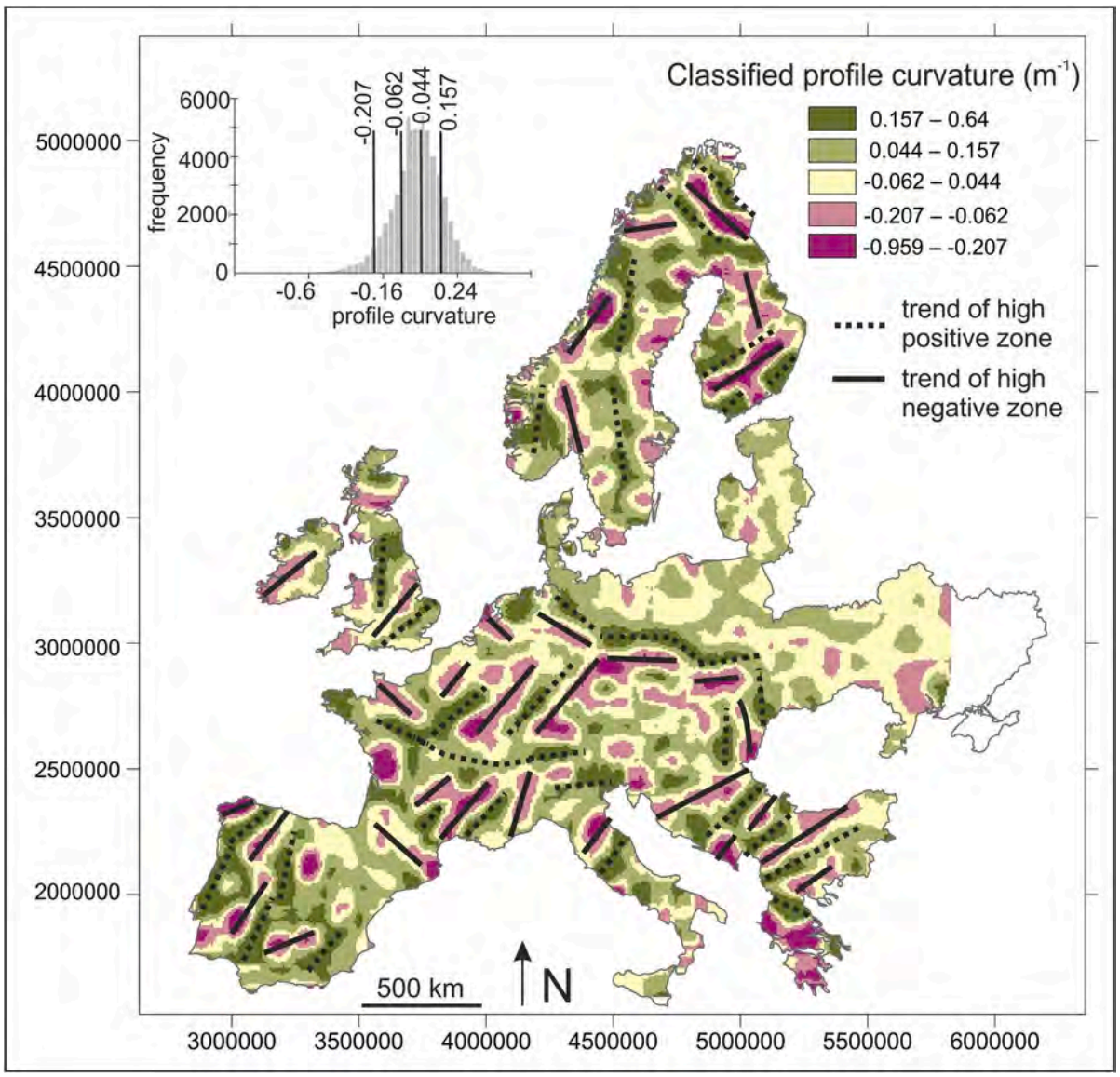

Fig. 13. Classified profile curvature map of Cr outlier-free data. The histogram displays classes identified by using natural break points. (For interpretation of the references to colour in this figure legend, the reader is referred to the web version of this article).

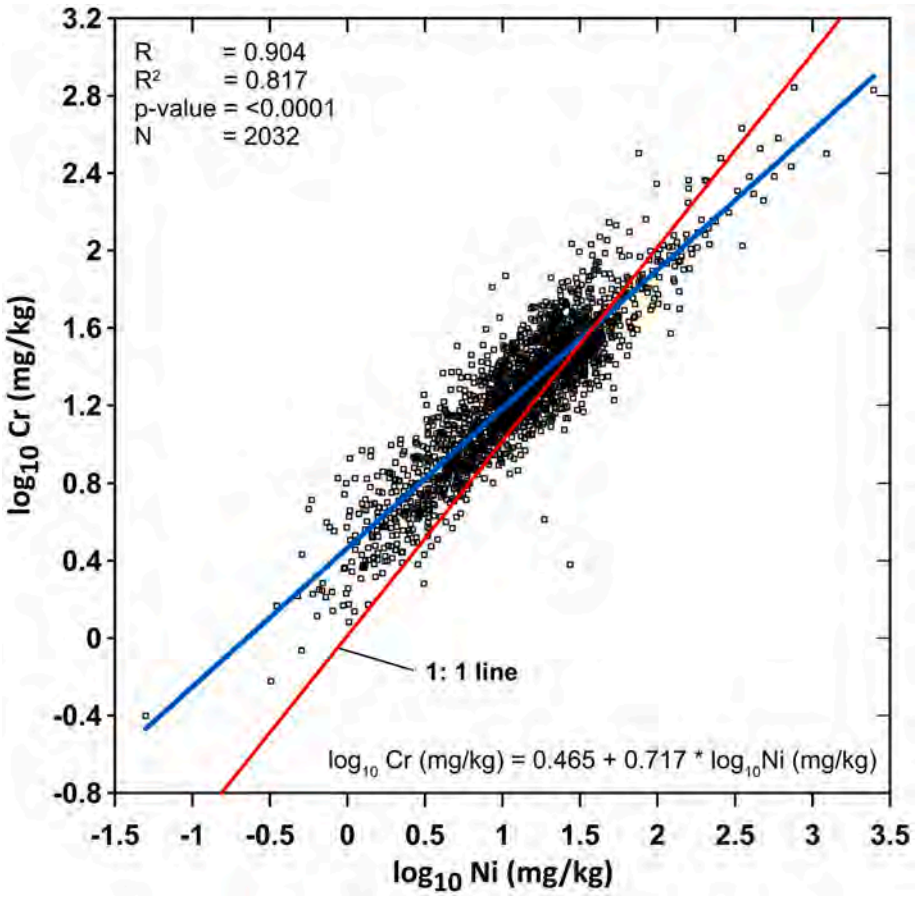

Fig. 14. Ni—Cr bivariate scatter plot; note the blue colour line and the high linear correlation coefficient ($R = 0.904$) between them. The axes are in the $\log_{10}$-scale. The number of data pairs is 2032. (For interpretation of the references to colour in this figure legend, the reader is referred to the web version of this article.)

zone crossing the NE-SW trending features in central Europe, extending from Normandy to the western edge of the Pannonian Basin. Slightly deviated, N-S-oriented spatial features were identified in the Iberian Peninsula and the western part of the Scandinavian Peninsula. The NW-SE trending pattern is scarce and occurs in northern Scandinavia and along the Pyrenees.

4. Discussion

During the early 1970s, digital image and processing techniques were developed (Condit and Chavez, 1979). The establishment of an image analysis facility has enabled applied geochemists to enhance their comprehensive research, especially in interpreting geochemical and geological characteristics (Green, 1984). However, recently, several artificial intelligence and machine learning algorithms have been used in the automation and interpretation of data and images. Digital image techniques can also extract valuable information related to geological and geochemical features and data, respectively. These methods enhance data, analyse pixel values, highlight patterns, and improve processing efficiency and accuracy by identifying trends, patterns and anomalies. While image processing and analysis offer several possibilities and benefits. There are, however, some challenges that might be considered in the interpretation of the results: for example, image noise, scale, resolution, algorithm selection, and optimisation. Thus, integrating image data with other geospatial information, such as various thematic maps and geological data, is essential (Kyser et al., 2015; Chen et al., 2020; Xu and Zhang, 2023).

This study uses digital spatial data techniques to identify new significant spatial patterns in interpolated element concentration maps. Additionally, previously identified features, including the last glaciation boundary (Reimann et al., 2014a; Albanese et al., 2015; Jordan et al., 2018.), have been quantitatively located and characterised. These methods enhance the understanding of geochemical pattern distributions by providing objective, reproducible insights into the spatial organisation of elemental concentrations. The integration of digital analysis enables a more precise delineation of geological boundaries and the detection of subtle geochemical trends that may have been overlooked using traditional mapping methods.

The statistical analysis of hot aqua regia extractable Cr concentrations in agricultural topsoil samples highlighted a distinctly right-skewed unimodal distribution, with 113 high outliers (Fig. 3). These outliers are primarily found in the Balkan Peninsula and the Apennine region (Fig. 6A). The highest Cr concentrations are associated with mafic-ultramafic rocks, such as ophiolite complexes (Fig. 4), where their median Cr value is 99.8 mg/kg (Fig. 4B). In contrast, low Cr values are concentrated in the Central and Eastern European Plain, with several local minima points aligned along a zone of glacial sands, defined by the southernmost boundary of the last glacial maximum (Figs. 4A, 6A, B, 7A, and B). In terms of the spatial distribution of Cr concentrations, mainland Europe can be subdivided into two large, distinct regions along the

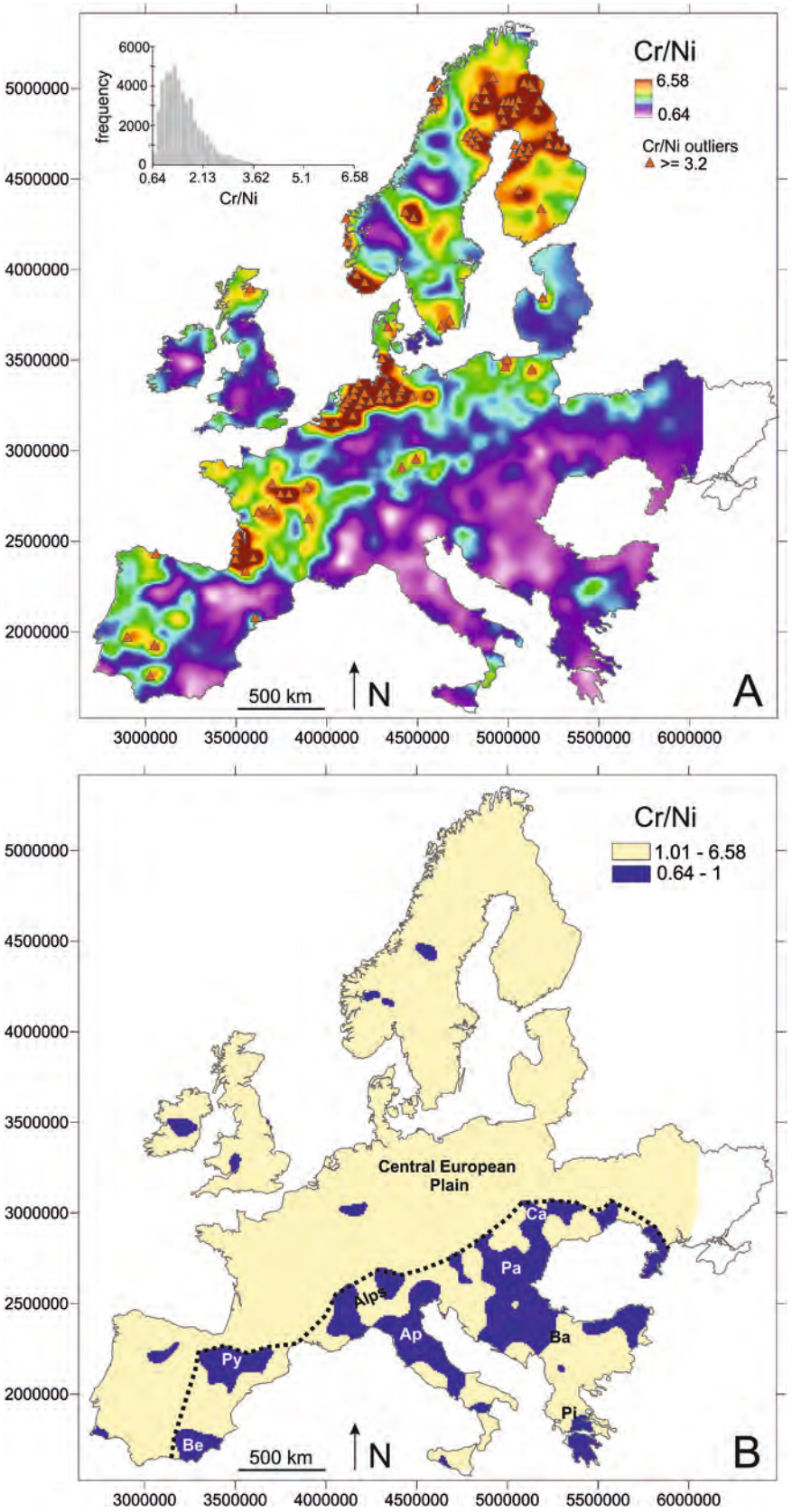

Fig. 15. (A) Cr/Ni ratio map using outlier-free data set. (B) Boolean-classified Cr/Ni ratio map. Note the sharp, NE-SW trending linear border between high and low Cr/Ni ratio zones. (For interpretation of the references to colour in this figure legend, the reader is referred to the web version of this article).

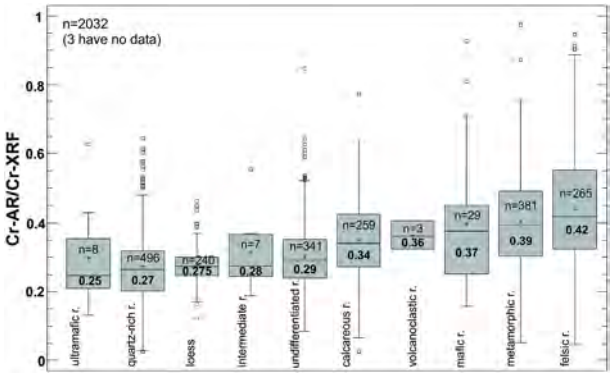

Fig. 16. Boxplots of Cr_{AR}/Cr_{XRF} ratios classified according to different parent lithologies at the sampling sites (n = 2032). Note the low ratios in agricultural soil samples over ultramafic and quartz-rich bedrock materials and the high ratios over felsic and metamorphic rocks.

southern limit of the last glaciation in central-northern Europe:

1) Low Cr concentrations occur in the northern and north-western parts of Europe over the glacial sands and loess, apart from the Archaean greenstone belts in the northern part of Scandinavia, the Oslo rift, and the Caledonian Mts (Figs. 4A, 6A, and 7).
2) Elevated Cr concentrations are present in the southern and south-eastern parts of Europe, especially over ophiolite rocks and their derivatives (Balkan Mts, northern Italy), terra rossa soil (northern Croatia), the Iberian Pyrite Belt, and the Baetic Mts (Figs. 4A, 6A, and 7).

In the second sub-region, regional-scale low Cr values were only identified in the Pannonian Basin over the young Late Miocene-Quaternary fluvial-lacustrine sediments and the northern part of the Iberian Peninsula (Fig. 7). The systematic digital image processing analysis revealed four outstanding spatial features in the Cr spatial distribution:

1) The hundreds of kilometres long NE-SW and the ENE-WSW trending zones are parallel to the alignment of local minima and maxima Cr values (Fig. 7A) and are characterised by a strong spatial anisotropy in the ENE-WSW direction (Fig. 9A) with distinct slope-breaks where the Cr values change abruptly (Profiles 1 and 2 in Figs. 7C and 13). They prevail in continental Europe and follow the trend of the Variscan and Alpine orogenies.
2) The E-W-oriented features are much longer and occur in well-defined zones. The most dominant is a homogeneous, north-facing zone with its northern border being parallel with the last continental glaciation maximum marked by the alignment of local minima points (Fig. 12A). The lowest Cr values (<12 mg/kg) are found north of the borderline (Figs. B and 7B) where the soil is acidic, with an average pH value of 5.66, and the prevailing climate is humid, thus promoting the mobility of chemical elements in soil (Braunschweiler and Koivisto, 2000; Salminen et al., 2005; De Vos et al., 2006; Fabian et al., 2014; Reimann et al., 2014a). The northern border of this area also marks a lithological boundary between glaciofluvial sediments and carbonate and semi-consolidated moraine formations (Fig. 4A). The alignment of local Cr maxima marks the southern border (Figs. 7A and 12A). Additionally, this southern boundary separates the glaciofluvial plains, such as the Central European Plain, from the outcrops of the Variscan and Alpine orogenies, including regions such as the Harz Mountains, Ardennes, Sudetes, and Carpathians. Outcrops of mafic and ultramafic rocks characterise these areas and host several Cr-ore mines and prospects (Cassard et al., 2012, 2015; Demetriades and Reimann, 2014). Furthermore, these E-W trending zones in central-northern Europe show a good agreement with some Hercynian fault zones.
3) The N-S-oriented features identified in the Scandinavian Peninsula run parallel to the Trans-Scandinavian Igneous Belt (TIB) and the Oslo Rift Zone (Or) (Figs. 7 and 8). They are both characterised by low Cr values due to the occurrence of felsic igneous rocks, i.e., granitic/(quartz) - monzogranitic to monzodioritic (Högdahl et al., 2004) in the TIB, and highly alkaline to tholeiitic basalt, trachyte and rhyolite in the Or (Neumann et al., 2004).
4) Finally, NW-SE-oriented features were identified in the Archaean greenstone belts of northern Fennoscandia, where there are several Cr-mineral occurrences (Figs. 1, 8, and 12).

The large-scale spatial features of Cr resemble the Ni patterns described by Jordan et al. (2018). Hence, the reason for selecting Cr to validate the use of digital image processing for the spatial pattern recognition and characterisation of continental-scale element spatial distribution in European agricultural topsoil. Due to their similar geochemical behaviour, they were compared using bivariate linear regression analysis (Fig. 14) and a ratio map (Fig. 15). The regression analysis reveals a significant linear correlation ($r = 0.904$ at the 95 % confidence level), confirming a strong association between the variables. The Cr/Ni ratio map exhibits a remarkable NE-SW trending continental-scale linear zone of thousands of kilometres across Europe along which the ratio changes sharply (Fig. 15). This linear feature separates the younger Alpine orogeny (e.g., Pyrenees, Alps, and Carpathians) in the south and south-east from the older Variscan and Caledonian structures in the northern part of Europe. The north-western part of Europe (e.g., Ardennes, Massif Central, Harz Mts) has higher Cr concentrations (Cr/Ni $\geq$ 1), while the south-eastern parts are characterised by lower Cr concentrations (Cr/Ni < 1), as compared to Ni. This border is perfectly delimited by the two classes of Cr/Ni ratios greater or less than unity (1), respectively (Fig. 15B).

To further explore the behaviour of Cr in the secondary agricultural topsoil environment, the ratio of Cr concentrations measured by hot aqua regia and XRF was also calculated. Firstly, the values of Cr_{AR}/Cr_{XRF} ratios were classified into parent material (lithological) categories (Fig. 16), which revealed that agricultural topsoil over quartz-rich cover sands, glaciofluvial sediments, loess, and ultramafic rocks have the lowest aqua regia extractable Cr concentrations. In contrast, topsoil samples over felsic and metamorphic rocks have the highest extractable Cr fraction (Fig. 16). This variation reflects differences in mineral composition and weathering behaviour, where quartz-rich and ultramafic substrates tend to immobilise chromium. At the same time felsic and metamorphic rocks may host more labile Cr forms. These lithological influences are significant to understanding regional geochemical mobility and bioavailability.

Secondly, the continental-scale spatial distribution of Cr_{AR}/Cr_{XRF} ratio was studied in a colour-enhanced map (Fig. 17), where low values suggest the presence of Cr in resistant primary minerals, such as chromite, that the total XRF analysis can detect. In contrast, high Cr_{AR}/Cr_{XRF} ratios indicate that Cr is associated with secondary clay minerals, organic matter and Fe-oxyhydroxides, which are more readily extractable by hot aqua regia. The map confirms the earlier finding that the parent material (lithology) has a significant control on the Cr_{AR}/Cr_{XRF}

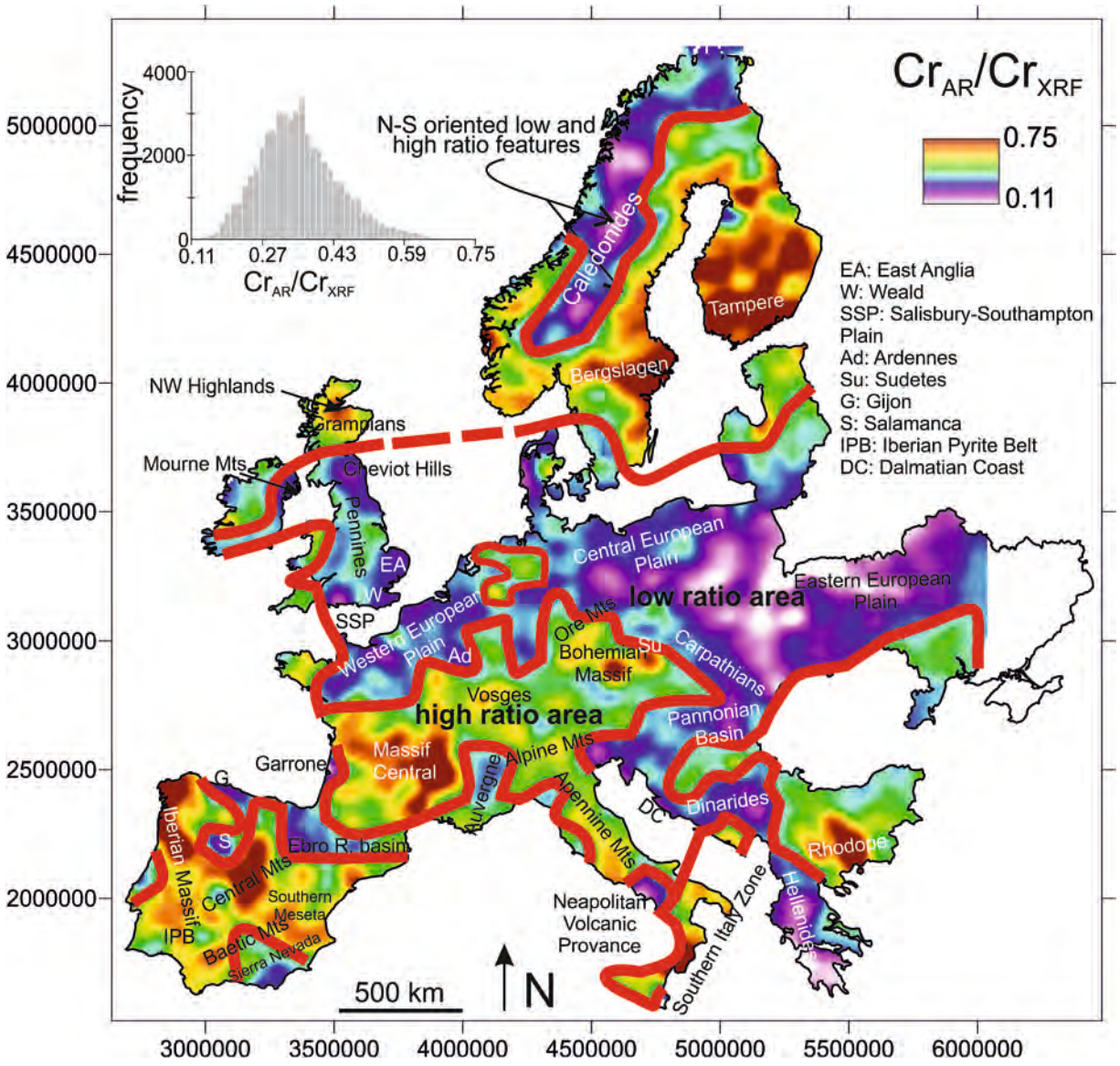

Fig. 17. Cr_{AR}/Cr_{XRF} ratio distribution map. The high Cr_{AR}/Cr_{XRF} ratios indicate that Cr is associated with secondary clay minerals, organic matter and Fe-oxyhydroxides, which are more easily extractable by hot aqua regia. The low ratio indicates the presence of Cr in resistant primary minerals such as chromite, which can be detected by total XRF analysis. Thick red lines separate high and low ratio Cr_{AR}/Cr_{XRF} areas. A detailed description of the spatial relationship of Cr_{AR}/Cr_{XRF} ratios to major geological units is presented in Appendix SM3 in the Supplementary Material. (For interpretation of the references to colour in this figure legend, the reader is referred to the web version of this article). (For interpretation of the references to colour in this figure legend, the reader is referred to the web version of this article.)

ratios. For example, the predominant low-ratio area is located in the north-central European plain, extending from Eastern Europe to Belgium, which is characterised by loess and coversands (Scheib et al., 2014). A detailed description of the spatial relationship of Cr_{AR}/Cr_{XRF} ratios to major geological units is presented in Appendix SM3 in the Supplementary Material. In Appendix SM4, the raw and processed data sets are provided.

5. Conclusions

This study introduces and validates the novel application of digital image processing methods for geochemical map analysis, using hot aqua regia extractable Cr concentrations in European agricultural topsoil, which differs significantly from Ni in terms of geochemistry and spectral response. The methodology is further expanded to bivariate analysis by analysing aqua regia extractable (Cr_{AR}) and XRF total (Cr_{XRF}) chromium concentrations together, in addition to the analysis of Ni—Cr ratios, showing the technique's adaptability and robustness. The demonstrated advancement is a significant methodological step, offering a fast, reproducible, and quantitative procedure for geochemical map analysis for environmental studies and mineral exploration.

The methodology progresses from basic statistical analysis to more advanced techniques, such as autocorrelation and geostatistical variogram analyses. These methods revealed new spatial distribution patterns of Cr concentrations in European agricultural soil not previously observed, such as multiple slope-break lines associated with the last continental glaciation and the trans-continental ENE-WSW and NE-SW zones across Central and Western Europe. This is the second study to delineate the geochemically defined boundary of the last continental glacial southern limit in a reproducible and quantitative way; the first being the Ni spatial patterns analysis (Jordan et al., 2018). The aspect analysis and identification of local Cr minima and maxima were particularly effective in recognising these patterns. Chromium demonstrates similar large-scale spatial patterns to Ni. In terms of the Cr/Ni

ratio, the north-western part of Europe has higher Cr concentrations (Cr/Ni ≥1), while the south and south-eastern parts have lower Cr concentrations (Cr/Ni <1). Finally, the digital processing of geochemical maps enables the quantitative comparison of the spatial patterns of chemical elements.

CRediT authorship contribution statement

Attila Petrik: Writing – review & editing, Writing – original draft, Visualization, Formal analysis, Conceptualization. **Gyozo Jordan:** Writing – review & editing, Writing – original draft, Validation, Investigation. **Ahmed Abdelaal:** Writing – review & editing, Visualization, Validation, Formal analysis. **Alecos Demetriades:** Writing – review & editing, Supervision, Methodology. **Benedetto De Vivo:** Writing – review & editing, Methodology, Formal analysis. **Stefano Albanese:** Writing – review & editing, Validation, Methodology. **Martiya Sadeghi:** Writing – review & editing, Methodology, Investigation.

Ethical responsibilities of authors

All authors have read, understood, and complied as applicable with the statement on "Ethical Responsibilities of Authors" as found in the Instructions for Authors.

Ethical approval for animal research

This article does not contain any studies on animals performed by any authors.

Funding

Not applicable.

Declaration of competing interest

The authors declare that they have no known competing financial interests or personal relationships that could have appeared to influence the work reported in this paper.

Acknowledgements

The GEMAS project represents a collaborative effort spearheaded by the EuroGeoSurveys Geochemistry Expert Group, with contributions from a diverse range of external institutions. These include organisations such as Alterra (The Netherlands), the Norwegian Forest and Landscape Institute, the Swiss Soil Monitoring Network Research Group, and Agroscope Reckenholz-Tänikon in Switzerland. Additional contributors span various ministries of environment and academic departments specialising in geosciences, chemistry, and mathematics across many European nations and New Zealand. Participation also came from ARCHE Consulting in Belgium and CSIRO Land and Water in Adelaide, Australia, alongside Eurometaux. Analytical operations carried out under GEMAS were partly funded by a consortium of industrial associations, including: Eurometaux, the European Borates Association, the European Copper Institute, the European Precious Metals Federation, and several international organisations such as the Antimony Association, Lead Association-Europe, Manganese Institute, Molybdenum Association, Tin Research Institute, Zinc Association, Cobalt Development Institute, and Chromium Institute. Further backing was provided by the REACH Selenium and Tellurium Consortium and the REACH Vanadium Consortium.

The authors extend their appreciation to the Directors of the participating Geological Surveys of Europe and affiliated institutions, whose efforts enabled comprehensive sampling across the continent within a narrow time frame. Acknowledgement is also due to the support received from the Kutató Kari Kiválósági Támogatás – Research Centre of Excellence – under grant number 1476-4/2016/FEKUT. Additionally, the financial assistance from the OTKA NKFIH Fund (Project No. SNN118101) is gratefully recognised.

Appendices. Supplementary data

Supplementary data to this article can be found online at https://doi.org/10.1016/j.gexplo.2025.107906.

Data availability

All data generated or treated during this study are included in this manuscript.

References

Abdaal, A., Jordan, G., Szilassi, P., 2013. Testing contamination risk assessment methods for mine waste sites. Water Air Soil Pollut. 224 (1416), 1–26. https://doi.org/10.1007/s11270-012-1416-x.

Albanese, S., Sadeghi, M., Lima, A., Cicchella, D., Dinelli, E., Valera, P., Falconi, M., Demetriades, A., De Vivo, B., The GEMAS Project Team, 2015. GEMAS: cobalt, Cr, Cu, and Ni distribution in agricultural and grazing land soil of Europe. J. Geochem. Explor. 154, 81–93.

Anderson, B.G., Borns Jr., H.W., 1997. The Ice Age World. Scandinavian Univ. Press, Oslo. ISBN 978-82-00-21810-4, 208 pp.

Berger, I., Frei, R., 2014. The fate of chromium during tropical weathering: a laterite profile from Central Madagascar. Geoderma 213, 521–532. https://doi.org/10.1016/j.geoderma.2013.09.004.

Birke, M., Reimann, C., Fabian, K., 2014. Analytical methods used in the GEMAS project. Chapter 5. In: Reimann, C., Birke, M., Demetriades, A., Filzmoser, P., O'Connor, P. (Eds.), Chemistry of Europe's Agricultural Soils — Part A: Methodology and Interpretation of the GEMAS Data Set, Geologisches Jahrbuch (Reihe B102). Schweizerbarth, Hannover, pp. 41–46. ISBN 978-3-510-96846-6.

Birke, M., Reimann, C., Rauch, U., Ladenberger, A., Demetriades, A., Jähne-Klingberg, F., Oorts, K., Dinelli, E., Halamic, J., 2017. GEMAS: cadmium distribution and its sources in agricultural and grazing land soil of Europe – original data versus clr-transformed data. J. Geochem. Explor. 173, 13–30. https://doi.org/10.1016/j.gexplo.2016.11.007.

Braunschweiler, H., Koivisto, S., 2000. Fate and Effects of Chemicals in the Nordic Environments Related to the Use of Biocides. Nordic Council of Ministers, Copenhagen. ISBN: 9789289304719, 9289304715, 135 pp.

Cassard, D., Bertrand, G., Maldan, F., Gaàl, G., Kaija, J., Aatos, S., Angel, J.M., Arvanitidis, N., Ballas, D., Billa, M., Christidis, C., Dimitrova, D., Eilu, P., Filipe, A., Gazea, E., Inverno, C., Kauniskangas, E., Maki, T., Matos, J., Meliani, M., Michael, C., Mladenova, V., Navas, J., Niedbal, M., Perantonis, G., Pyra, J., Santana, H., Serafimovski, T., Serrano, J.J., Strengell, J., Tasev, G., Tornos, F., Tudor, G., 2012. ProMine pan-European Mineral Deposit database: a new dataset for assessing primary mineral resources in Europe. In: Workshop on: Mineral Resources Potential Maps: a Tool for Discovering Future Deposits. 12th-14th March 2012, Nancy, France, Proceedings, pp. 9–13.

Cassard, D., Bertrand, G., Billa, M., Serrano, J.-J., Tourlière, B., Angel, J.-M., Gaál, G., 2015. ProMine mineral databases: new tools to assess primary and secondary mineral resources in Europe. In: Weihed, P. (Ed.), 3D, 4D and Predictive Modelling of Major Mineral Belts in Europe, Mineral Resource Reviews. Springer International Publishing, Switzerland, pp. 9–58. https://doi.org/10.1007/978-3-319-17428-0_2.

Chen, J., Mao, Z., Zhao, Y., Zhang, C., Jiang, S., 2020. The geochemical data imaging and application in geoscience: taking the Northern Daxinganling metallogenic belt as an example. In: Mazadiego, F.L., Garcia, E. De M., Barrio-Parra, F., Izquierdo-Diaz, M. (Eds.), Applied Geochemistry with Case Studies on Geological Formations, Exploration Techniques and Environmental Issues. IntechOpen. https://doi.org/10.5772/intechopen.84725, 18 pp.

Condit, C.D., Chavez, P.S., 1979. Basic concepts of computerized digital image processing for geologists. Geol. Den. Surv. Bull. 1462, 16. https://pubs.usgs.gov/bul/1462/report.pdf.

Cressie, N., 1993. Statistics for Spatial Data. J. Wiley & Sons, New York, NY, 928 pp.

Davis, J.C., 2011. Statistics and Data Analysis in Geology. J. Wiley & Sons, India. ISBN: 9788126530083, 656 pp.

De Vos, W., Tarvainen, T., Salminen, R., Reeder, S., De Vivo, B., Demetriades, A., Pirc, S., Batista, M.J., Marsina, K., Ottesen, R.T., O'Connor, P.J., Bidovec, M., Lima, A., Siewers, U., Smith, B., Taylor, H., Shaw, R., Salpeteur, I., Gregorauskiene, V., Halamic, J., Slaninka, I., Lax, K., Gravesen, P., Birke, M., Breward, N., Ander, E.L., Jordan, G., Duris, M., Klein, P., Locutura, J., Bellan, A., Pasieczna, A., Lis, J., Mazreku, A., Gilucis, A., Heitzmann, P., Klaver, G., Petersell, V., 2006. Geochemical Atlas of Europe: Part 2 - Interpretation of Geochemical Maps, Additional Tables, Figures, Maps, and Related Publications. Geological Survey of Finland, Espoo, 692 pp. http://weppi.gtk.fi/publ/foregsatlas/.

Delina, R.E., Arcilla, C., Otake, T., Garcia, J.J., Tan, M., Akane Ito, A., 2020. Chromium occurrence in a nickel laterite profile and its implications to surrounding surface waters. Chem. Geol. 558, 119863. https://doi.org/10.1016/j.chemgeo.2020.119863.

Demetriades, A., Reimann, C., 2014. Mineral deposits in Europe. Chapter 3. In: Reimann, C., Birke, M., Demetriades, A., Filzmoser, P., O'Connor, P. (Eds.), Chemistry of Europe's Agricultural Soils – Part B: General background Information and Further Analysis of the GEMAS data set, Geologisches Jahrbuch (Reihe B103). Schweizerbarth, Hannover, pp. 71––78. ISBN 978-3-510-96847-3.

Demetriades, A., Reimann, C., Filzmoser, P., 2014. Evaluation of GEMAS project quality control results. Chapter 6. In: Reimann, C., Birke, M., Demetriades, A., Filzmoser, P., O'Connor, P. (Eds.), Chemistry of Europe's Agricultural Soils – Part A: Methodology and Interpretation of the GEMAS Data Set, Geologisches Jahrbuch (Reihe B102). Schweizerbarth, Hannover, pp. 47–60. ISBN 978-3-510-96846-6.

Dürr, H.H., Meybeck, M., Dürr, S.H., 2005. Lithologic composition of the Earth's continental surfaces derived from a new digital map emphasizing riverine material transfer. Glob. Biogeochem. Cycles 19 (4), 1–22. https://doi.org/10.1029/2005GB002515/epdf.

EC, 2006. Regulation (EC) No 1907/2006 of The European Parliament and of the Council of 18 December 2006 concerning the Registration, Evaluation, Authorisation and Restriction of Chemicals (REACH), establishing a European Chemicals Agency, amending Directive 1999/45/EC and repealing Council Regulation (EEC) No 793/93 and Commission Regulation (EC) No. 1488/94 as well as Council Directive 76/769/EEC and Commission Directives 91/155/EEC, 93/67/EEC, 93/105/EC and 2000/21/EC, 396. Off. J. Eur. Union L, Luxembourg, 518 pp. https://eur-lex.europa.eu/LexUriServ/LexUriServ.do?uri=OJ%3AL%3A2007%3A136%3A0003%3A0280%3AEN%3APDF&utm_source=chatgpt.com.

Ertani, A., Mietto, A., Borin, M., Nardi, S., 2017. Chromium in agricultural soils and crops: a review. Water Air Soil Pollut. 228, 190. https://doi.org/10.1007/s11270-017-3356-y.

ESRI, 2011. ArcGIS Desktop: Release 10. Environmental Systems Research Institute, Redlands, CA.

EuroGeoSurveys Geochemistry Working Group, 2009. EuroGeoSurveys Geochemical Mapping of Agricultural and Grazing Land Soil of Europe (GEMAS): Field Manual. NGU Report 2008-038. Geological Survey of Norway, Trondheim, Norway, 46 pp. https://static.ngu.no/upload/Publikasjoner/Rapporter/2008/2008_038.pdf.

Fabian, C., Reimann, C., Fabian, K., Birke, M., Baritz, R., Haslinger, E., The GEMAS Project Team, 2014. GEMAS: Spatial distribution of the pH European agricultural and grazing land soil. Appl. Geochem. 48, 207–216.

Gonzalez, R.C., Woods, R.E., 1993. Digital Image Processing, Third edition. Pearson Prentice Hall, Upper Saddle River. 943 pp.

Gosar, M., Šajn, R., Teršič, T., 2016. Distribution pattern of mercury in the Slovenian soil: Geochemical mapping based on multiple geochemical datasets. J. Geochem. Explor. 167, 38–48.

Green, P.M., 1984. Digital image processing of integrated geochemical and geological information. J. Geol. Soc. Lond. 141 (5), 941–949. https://doi.org/10.1144/gsjgs.141.5.0941.

Guibas, L., Stolfi, J., 1985. Primitives for the manipulation of general subdivisions and the computation of Voronoi diagrams. ACM Trans. Graph. 4 (2), 74–123.

Hartwich, R., Baritz, R., Fuchs, M., Krug, D., Thiele, S., 2005. Explanation to the Soil Regions Map of the European Union and Adjacent Countries 1:5,000,000 (Version 2.0). European Soil Bureau, Luxembourg research reports.

Högdahl, K., Andersson, U.B., Eklund, O. (Eds.), 2004. The Transscandinavian Igneous Belt (TIB) in Sweden: A Review of Its Character and Evolution. Geological Survey of Finland. Special Paper 37, 123 pp. https://tupa.gtk.fi/julkaisu/specialpaper/sp_037.pdf.

Hseu, Z.-Y., Zehetner, F., Fujii, K., Watanabe, T., Nakao, A., 2018. Geochemical fractionation of chromium and nickel in serpentine soil profiles along a temperate to tropical climate gradient. Geoderma 327, 97–106. https://doi.org/10.1016/j.geoderma.2018.04.030.

Hu, Z., Gao, S., 2008. Upper crustal abundances of trace elements: a revision and update. Chem. Geol. 253 (3–4), 205–221. https://doi.org/10.1016/j.chemgeo.2008.05.010.

Jordan, G., Petrik, A., De Vivo, B., Albanese, S., Demetriades, A., Martiya Sadeghi, M., 2018. GEMAS: spatial analysis of the Ni distribution on a continental-scale using digital image processing techniques on European agricultural soil data. J. Geochem. Explor. 186, 143–157. https://doi.org/10.1016/j.gexplo.2017.11.011.

Kabata-Pendias, A., Pendias, H., 2001. Trace Elements in Soils and Plants, 3rd edition. CRC Press, Boca Raton. ISBN: 0849315751, 403 p.

Kürzl, H., 1988. Exploratory data analysis: recent advances for the interpretation of geochemical data. J. Geochem. Explor. 30, 309–322.

Kyser, K., Barr, J., Ihlenfeld, C., 2015. Applied geochemistry in mineral exploration and mining. Elements 11 (4), 241–246. https://doi.org/10.2113/gselements.11.4.241.

Li, Z., Zhu, C., Gold, C., 2004. Digital Terrain Modeling: Principles and Methodology. CRC Press, 340 pp.

Mann, H.B., Whitney, D.R., 1947. On a test of whether one of two random variables is stochastically larger than the other. Ann. Math. Stat. 18 (1), 50–60.

Mielke, J.E., 1979. Composition of the earth's crust and distribution of the elements. In: Siegel, F.R. (Ed.), Review of Research on Modern Problems in Geochemistry, Earth Science Series, 16. International Association for Geochemistry and Cosmochemistry, Paris, pp. 13–37.

Négrel, P., Ladenberger, A., Reimann, C., Birke, M., Demetriades, A., Sadeghi, M., 2019. GEMAS: Geochemical background and mineral potential of emerging tech-critical elements in Europe revealed from low-sampling density geochemical mapping. Appl. Geochem. 111, 104425. https://doi.org/10.1016/j.apgeochem.2019.104425.

Neumann, E.-R., Wilson, M., Heeremans, M., Spencer, E.A., Obst, K., Timmerman, M.J., Kirstein, L., 2004. Carboniferous-Permian rifting and magmatism in southern Scandinavia, the North Sea and northern Germany: a review. In: Wilson, M., Neumann, E.-R., Davies, G.R., Timmerman, M.J., Heeremans, M., Larsen, B.T. (Eds.), Permo-Carboniferous Magmatism and Rifting in Europe, Special Publication 223. Geological Society, London, pp. 11–40. https://doi.org/10.1144/GSL.SP.2004.223.01.02.

Plant, J.A., Reeder, S., Salminen, R., Smith, D.B., Tarvainen, T., De Vivo, B., Petterson, M. G., 2003. The distribution of uranium over Europe: geological and environmental significance. Applied Earth Science, Trans. Inst. Min. Metall. B. 112, B221–B238.

Plant, J.A., Whittaker, A., Demetriades, A., De Vivo, B., Lexa, J., 2005. The geological and tectonic framework of Europe. In: Salminen, R., Batista, M.J., Bidovec, M., Demetriades, A., De Vivo, B., De Vos, W., Duris, M., Gilucis, A., Gregorauskiene, V., Halamic, J., Heitzmann, P., Lima, A., Jordan, G., Klaver, G., Klein, P., Lis, J., Locutura, J., Marsina, K., Mazreku, A., O'Connor, P.J., Olsson, S.Å., Ottesen, R.-T., Petersell, V., Plant, J.A., Reeder, S., Salpeteur, I., Sandström, H., Siewers, U., Steenfelt, A., Tarvainen, T. (Eds.), FOREGS – Geochemical Atlas of Europe. Part 1: Background, Information, Methodology and Maps. Geological Survey of Finland, Espoo, pp. 23–42. http://weppi.gtk.fi/publ/foregsatlas/articles/Geology.pdf.

Ramsey, M.H., 1998. Sampling as a source of measurement uncertainty: techniques for quantification and comparison with analytical sources. J. Anal. At. Spectrom. 13, 97–104.

Ramsey, M.H., Ellison, S.L.R., Rostron, P. (Eds.), 2019. Eurachem/EUROLAB/ CITAC/ Nordtest/AMC Guide: Measurement Uncertainty Arising from Sampling: A Guide to Methods and Approaches, Second edition. Eurachem. 104 pp. https://www.eurachem.org/images/stories/Guides/pdf/UfS_2019_EN_P2.pdf.

Reimann, C., Caritat, P. de, 1998. Chemical Elements in the Environment - Factsheets for the Geochemist and Environmental Scientist. Springer-Verlag, Berlin-Heidelberg. ISBN: 978-3-642-72018-5, 398 pp.

Reimann, C., Demetriades, A., Eggen, O.A., Filzmoser, P., EuroGeoSurveys Geochemistry Group, 2009. The EuroGeoSurveys Geochemical Mapping of Agricultural and Grazing Land Soils Project (GEMAS) - Evaluation of Quality Control Results of Aqua Regia Extraction Analysis. NGU Report 2009.049. Geological Survey of Norway, Trondheim, 94 pp. https://static.ngu.no/upload/Publikasjoner/Rapporter/2009/2009_049.pdf.

Reimann, C., Demetriades, A., Eggen, O.A., Filzmoser, P., The EuroGeoSurveys Geochemistry Expert Group, 2011. The EuroGeoSurveys Geochemical Mapping of Agricultural and Grazing Land Soils Project (GEMAS) – Evaluation of Quality Control Results of Total C and S, Total Organic Carbon (TOC), Cation Exchange Capacity (CEC), XRF, pH, and Particle Size Distribution (PSD) Analysis. Geological Survey of Norway, Trondheim. NGU report 2011.043. https://static.ngu.no/upload/Publikasjoner/Rapporter/2011/2011_043.pdf.

Reimann, C., Flem, B., Fabian, K., Birke, M., Ladenberger, A., Négrel, P., Demetriades, A., Hoogewerff, J., The GEMAS Project Team, 2012. Lead and lead isotopes in agricultural soils of Europe - the continental perspective. Appl. Geochem. 27, 532–542. https://doi.org/10.1016/j.apgeochem.2011.12.012.

Chemistry of Europe's agricultural soils - part A: Methodology and interpretation of the GEMAS data set. In: Reimann, C., Birke, M., Demetriades, A., Filzmoser, P., O'Connor, P. (Eds.), 2014a. Geologisches Jahrbuch (Reihe B 102). Schweizerbarth, Hannover, 528 pp. https://www.schweizerbart.de/publications/detail/isbn/9783510968466.

Chemistry of Europe's agricultural soils – part B: general background information and further analysis of the GEMAS data set. In: Reimann, C., Birke, M., Demetriades, A., Filzmoser, P., O'Connor, P. (Eds.), 2014b. Geologisches Jahrbuch (Reihe B 103). Hannover, Schweizerbarth, 352 pp. https://www.schweizerbart.de/publications/detail/isbn/9783510968473/Geologisches_Jahrbuch_Reihe_B_Heft_B103_Chemistry.

Reimann, C., Demetriades, A., Birke, M., Filzmoser, P., O'Connor, P., Halamić, J., Ladenberger, A., The GEMAS Project Team, 2014c. Distribution of elements/parameters in agricultural and grazing land soil of Europe. Chapter 11. In: Reimann, C., Birke, M., Demetriades, A., Filzmoser, P., O'Connor, P. (Eds.), Chemistry of Europe's Agricultural Soils – Part A: Methodology and Interpretation of the GEMAS data set, Geologisches Jahrbuch (Reihe B102). Schweizerbarth, Hannover, pp. 103–474. ISBN 978-3-510-96846-6.

Riley, S.J., Degloria, S.D., 1999. A terrain ruggedness index that quantifies topographic heterogeneity. Int. J. Therm. Sci. 5 (1–4), 23–27.

Saha, R., Nandi, R., Saha, B., 2011. Sources and toxicity of hexavalent chromium. J. Coord. Chem. 64 (10), 1782–1806.

Salminen, R., Batista, M.J., Bidovec, M., Demetriades, A., De Vivo, B., De Vos, W., Duris, M., Gilucis, A., Gregorauskiene, V., Halamic, J., Heitzmann, P., Lima, A., Jordan, G., Klaver, G., Klein, P., Lis, J., Locutura, J., Marsina, K., Mazreku, A., O'Connor, P.J., Olsson, S.Å., Ottesen, R.-T., Petersell, V., Plant, J.A., Reeder, S., Salpeteur, I., Sandström, H., Siewers, U., Steenfelt, A., Tarvainen, T., 2005. FOREGS Geochemical Atlas of Europe, Part 1: Background Information, Methodology and Maps. Geological Survey of Finland, Espoo, 526 pp. http://weppi.gtk.fi/publ/foregsatlas/.

Scheib, J., Flight, D.M.A., Birke, M., Tarvainen, T., Locutura, J., GEMAS Project Team, 2012. The geochemistry of niobium and its distribution and relative mobility in agricultural soils of Europe. Geochem. Explor. Environ. Anal. 12, 293–302. https://doi.org/10.1144/geochem2011-096.

Scheib, A.J., Birke, M., Dinelli, E., GEMAS Project Team, 2014. Geochemical evidence of aeolian deposits in European soils. Boreas 43 (1), 175–192. https://doi.org/10.1111/bor.12029.

Spielhagen, R.F., Baumann, K.-H., Erlenkeuser, H., Nowaczyk, N.R., Norgaard-Pedersen, N., Vogt, C., Weiel, D., 2004. Arctic Ocean deep-sea record of Northern Eurasian ice sheet history. Quat. Sci. Rev. 23 (11–13), 1455–1483.

Svendsen, J.I., Alexanderson, H., Astakhov, V.I., Demidov, I., Dowdeswell, J.A., Funder, S., Gataullin, V., Henriksen, M., Hjort, C., Houmark-Nielsen, M., Hubberten, H.W., Ingolfsson, O., Jacobsson, M., Kjaer, K., Larsen, E., Lokrantz, H., Lunkka, J.P., Lysa, A., Mangerud, J., Matioushkov, A., Murray, A., Möller, P., Niessen, F., Nikolskaya, O., Polyak, L., Saarnisto, M., Siegert, C., Siegert, M.J.,

Spielhagen, R.F., Stein, R., 2004. Late quaternary ice sheet history of northern Eurasia. Quat. Sci. Rev. 23 (11), 1229–1272.
Tarvainen, T., Albanese, S., Birke, M., Ponavic, M., Reimann, C., The GEMAS Project Team, 2013. Arsenic in agricultural and grazing land soils of Europe. Appl. Geochem. 28, 2–10. https://doi.org/10.1016/j.apgeochem.2012.10.005.
Tarvainen, T., Smith, S.M., Filzmoser, P., Demetriades, A., Bogatyrev, I., Albanese, S., 2022. Data management and map production. Chapter 9. In: Demetriades, A., Johnson, C.C., Smith, D.B., Ladenberger, A., Adánez Sanjuan, P., Argyraki, A., Stouraiti, C., Caritat, P. de, Knights, K.V., Prieto Rincón, G., Simubali, G.N. (Eds.), International Union of Geological Sciences Manual of Standard Methods for Establishing the Global Geochemical Reference Network, 2. IUGS Commission on Global Geochemical Baselines, Athens, Hellenic Republic, pp. 457–485. https://doi.org/10.5281/zenodo.7307696. Special Publication.
Tukey, J.W., 1977. Exploratory Data Analysis. Addison-Wesley, 506 pp.
Wedepohl, K.H., 1978. Handbook of Geochemistry, Volume I-IV. Springer-Verlag, Berlin, pp. 1969–1978. ISSN: 0072-9817.
Xu, H., Zhang, C., 2023. Development and applications of GIS-based spatial analysis in environmental geochemistry in the big data era. Environ. Geochem. Health 45, 1079–1090. https://doi.org/10.1007/s10653-021-01183-8.